Development and preliminary validation of TIFONE, a design-oriented code for the inter-wrapper flow and heat transfer in liquid-metal-cooled reactors

Nuclear Engineering and Design 428 (2024) 113469

Contents lists available at ScienceDirect

Nuclear Engineering and Design

journal homepage: www.elsevier.com/locate/nucengdes

Development and preliminary validation of TIFONE, a design-oriented code for the inter-wrapper flow and heat transfer in liquid-metal-cooled reactors

G.F. Nallo [a,*], F. Lodi [b], G. Grasso [b]

[a] NEMO Group, Dipartimento Energia, Politecnico di Torino, Corso Duca degli Abruzzi 24, Torino, 10129, Italy
[b] Italian National Agency for New Technologies, Energy and Sustainable Economic Development (ENEA), Via Martiri di Monte Sole 4, Bologna, 40129, Italy

ARTICLE INFO

Keywords:
Liquid-metal-cooled reactors
Core thermal-hydraulics
Inter-wrapper flow
Design-oriented code
Code development

ABSTRACT

Among the goals of the core design for Lead-cooled Fast Reactors (LFRs) exploiting the closed Sub-Assembly (SA) option, cold by-passes should be minimised and excessive thermal gradients among opposite faces of the assembly ducts prevented. To this aim, given an Inter-Wrapper (IW) gap determined by the core thermo-mechanical design, a suitable coolant flow outside the assemblies themselves must be guaranteed. Moreover, the designer has the opportunity to introduce flow restrictions to tune the intra-wrapper flow fraction at the SA level, possibly allowing to reduce temperature differences at the outlet of the assemblies.

Therefore, the designer needs to be aware of the axial and radial temperature profiles of the IW coolant throughout the whole core (i.e., including all core SAs), as well as of the axial and perimetrical temperature profiles of the wrapper of each SA. Notably, the possibly different temperature values of each side of the wrapper itself should be assessed, since they could induce SA bowing. To address these needs, a Design-Oriented Code (DOC), TIFONE, was developed and verified in compliance with current best practices in terms of software quality assurance.

TIFONE adopts the sub-channel method, leading to a sufficient level of spatial resolution while retaining the key features of a DOC, namely equilibrium, a low computational time and a clear application domain. The paper describes the code structure, governing equations and solution method. It also reports the preliminary validation of TIFONE against data from inter-wrapper flow and heat transfer experiments performed in the frame of the SESAME project at the THESYS loop within the KALLA laboratory, confirming the code capability to reproduce the measured data in its anticipated validity domain.

1. Introduction

Heavy-Liquid-Metal-Cooled Reactors (HLMCRs) are at the centre of an increasing international attention as well as being one of the technologies fostered by the Generation IV International Forum (GIF). HLMCRs are characterised by a fast neutron spectrum and have the potential to meet the GIF goals in terms of safety, sustainability and cost-effectiveness with minimisation of long-lived radioactive waste and reduced proliferation risks.

Specifically, the core design of HLMCRs is a multidisciplinary task, dealing with many deeply interconnected physical/engineering parameters. It can be logically subdivided into Thermo-Mechanic (TM), Thermal-Hydraulic (TH) and Neutronic (NE) design, based on the three most relevant physics involved. Safety aspects must be embedded from the early stages, according to the core design approach of Generation IV technologies. During the design phase process, Design-Oriented Codes (DOCs) are used to effectively inform design decisions by highlighting the relations between the parameters entering the problem. DOCs are characterised by a relatively short time required to prepare and run calculations, and by a clearly identified application domain.

For HLMCR cores adopting *wrapped* Sub-Assemblies (SAs) and thus inherently characterised by the presence of an Inter-Wrapper (IW) (or *bypass*) region, the core design goals include the minimisation of cold bypasses and of excessive thermal gradients among opposite faces of the assembly ducts (IAEA, 2012). To achieve these goals, a suitable coolant flow outside the assemblies themselves must be guaranteed, compatibly with the IW gap, the width of the latter being established by the core thermo-mechanical design. Moreover, for wrapped assemblies, the possibility of tuning the intra-wrapper flow fraction at the SA level through orificing arises, giving the designer an extra degree of freedom for levelling thermal gradients at the assemblies' outlet. Therefore, the design process requires knowledge of the axial and radial coolant temperature profiles in the IW gaps throughout the whole core (i.e., including all core SAs), as well as of the axial and perimetrical wrapper temperature profiles, and notably the (possibly) different values of

* Corresponding author.
E-mail address: giuseppefrancesco.nallo@polito.it (G.F. Nallo).

https://doi.org/10.1016/j.nucengdes.2024.113469
Received 4 January 2024; Received in revised form 6 June 2024; Accepted 10 July 2024
Available online 24 July 2024

each side of the wrapper itself which could induce SA bowing. The above-mentioned requirements point out the need for a DOC capable of solving the whole-core Thermal-Hydraulics (TH), including the IW flow and heat transfer.

A literature review pointed out the existence of at least four TH codes suitable for the full-core analysis of HLMCRs: COBRA-WC (George et al., 1980), NETFLOW (Mochizuki, 2007), SUPERENERGY-II (Basehore and Todreas, 1980) and its most recent version SE2-ANL (Yang and Yacout, 1995). However, COBRA-WC and NETFLOW are rather complex tools aimed at transient analyses, hence more suitable for the verification phase than for the design phase. SUPERENERGY-II and SE2-ANL match more closely the definition of DOC provided above, especially thanks to their steady state nature, but the IW flow is treated in a somewhat simplified way.

Very recent efforts to tackle the IW flow and heat transfer model should also be here mentioned. In Yue et al. (2018), an IW model with low radial resolution (at the level of the single SA face) is presented, which was coupled to the transient THACS code and validated against experiments from Phénix and EBR-II reactors. In Deng et al. (2020), instead, the target was to develop a multi-SA code with IW capabilities for lead-cooled and LBE-cooled reactors. To this aim, a two-step procedure was employed, which adopts a coarse multi-SA model to locate the hottest SA and then performs a detailed calculation within it. Finally, in Luo et al. (2022) a new whole-core code for LMCRs, KMC-FBC, is presented. This code is capable to adopt both a simple two-steps model and a more complex pin-by-pin model which is similar to the one employed in SE2-ANS. Flowing IW channels are considered, even though radial exchange within the IW region is neglected for the sake of simplicity.

In view of this literature review, to the best of the authors' knowledge, it can be stated that the availability of validated DOCs for the TH calculation of the full core of HLMCRs including the IW flow and heat transfer which features the required level of detail is currently very scarce, if existing. However, it should be mentioned that single-SA TH DOCs such as ANTEO+ are able to account for the presence of the surrounding IW coolant, even though they do not account for inter-SA heat transfer (Lodi and Grasso, 2016, 2017).

These considerations motivated the design and development of a new DOC, TIFONE, to solve the IW flow and heat transfer problem. This can be seen as a first step towards the development of a DOC for the core TH of HLMCRs. TIFONE has been preliminarily validated against experimental data from IW flow and heat transfer experiments performed in the frame of the SESAME project at the THESYS loop within KALLA laboratory.

The paper is organised as follows: the approach followed for the TIFONE development, the governing equations and solution method are described in Section 2. The constitutive relations adopted to close the set of conservation equations are then listed in Section 3. The results of the preliminary validation campaign are shown and commented in Section 4. Finally, conclusions and perspectives are outlined.

2. The TIFONE code

2.1. Code design overview

The name TIFONE stems from an Italian acronym (Termo-Idraulica delle Fughe che Occorrono nel Nocciolo fra gli Elementi, meaning "thermal-hydraulics of the bypass flow occurring in the core among the SAs"). Consistently with its name, TIFONE targets the TH simulation of reactor cores cooled by liquid metals with closed SAs in hexagonal geometry. Indeed, in view of the possibility to take advantage of available experimental data from sodium-cooled reactors and experiments, TIFONE was not limited to heavy liquid metals.

The TIFONE calculation domain extends radially over the IW region of the entire core, and axially between the dividing and the merging points of the inter- and intra-SA coolant flows, see Fig. 1 (left). Fig. 1 (right) shows the calculation domain corresponding to the inter-wrapper gap between several SAs, consisting in a thin region (a few mm) extending axially and radially over the whole core.

Consistently with the features of a DOC, a clear validity domain was defined beforehand. TIFONE targets the simulation of the IW flow and heat transfer in forced and mixed convection regime, where an axially dominant flow is present. Conversely, buoyancy dominated free convection situations, possibly inducing flow re-circulations, cannot be simulated. This limits the applicability of the current version of TIFONE to core designs specifically featuring an IW flow which is fed with part of the total core flow rate, thus excluding situations where the IW is only fed by recirculations from the upper plenum.

The Sub-Channel (SC) approach was chosen, since it allows to achieve a sufficient level of spatial resolution while retaining the key features of a DOC, namely equilibrium, a low computational time and a clear application domain. TIFONE solves the inter-SA coolant mass, energy and momentum equations, as well as the convection equations between the coolant and the wrapper. The required inputs are the core geometry, as established by the core thermo-mechanical design, the axial and perimetrical distribution of the heat flux flowing out of all the SAs in the core, the coolant inlet temperature and flow rate, and the fraction of the core inlet mass flow rate flowing within the IW region.

The code was developed according to the Software Quality Management System in place within ENEA's SICNUC division, incorporating guidelines from standards such as ISO/IEC/IEEE 12207 (ISO 12207:2017, 2017). After an initial planning phase, a software requirements specification document was produced. A software design compliant with the specified requirements was then developed, discussed and approved before starting the code development phase, which includes testing and verification of the code compliance with the specified requirements. Finally, a preliminary code validation was performed against available experimental data.

2.2. Spatial discretisation

The gap between each couple of SAs is radially subdivided into a number of *edge SC*, indicated in red in Fig. 2. The region between three hydraulically connected gaps is instead associated to a single *corner SC*, indicated in blue in Fig. 2. This choice allows to take into account the TH connection between adjacent gaps, as well as to take advantage of the most detailed information available for the heat crossing the wrapper. This discretisation has been adopted in Basehore and Todreas (1980), as well as in the simplified treatment of the IW thermal-hydraulics in the ANTEO+ code. The possibility to further split the IW gap between the neighbouring assemblies – with boundaries at the gap centreline – was instead disregarded since it would provide an unnecessary level of detail while potentially hindering code stability (Basehore and Todreas, 1980).

Each SC is then axially subdivided in a number of control volumes with an user-specified distribution. The code is therefore capable of determining the axial variation of the quantities of interests.

2.3. Governing equations

2.3.1. Assumptions

TIFONE aims at the TH calculation of the IW coolant over the full core of an HLMCR, as well as of the wrapper outer temperature for each SA. To this purpose, the SC method is adopted, using the above described discretisation. The underlying assumptions of the SC method, as indicated in Todreas and Kazimi (1990), are:

- the control volume is fixed and common to all the conservation equations, except the transverse momentum equation;
- the transverse flow "loses memory of" his original direction when passing from an SC to the neighbouring one.

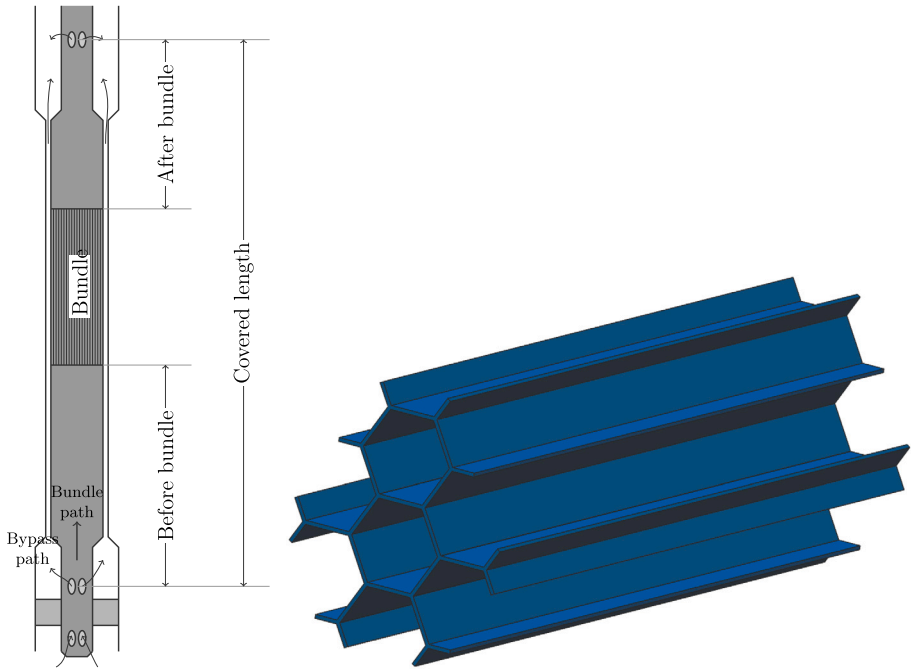

Fig. 1. Schematic of the bypass flow domain, adapted from Lodi (2017) (left) and representation of the inter-wrapper flow domain (right).

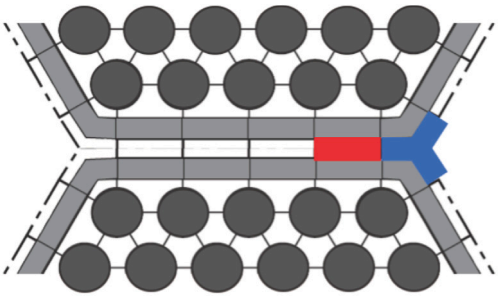

Fig. 2. Inter-assembly gap SC subdivision options.

Additional simplifying assumptions have been adopted in the present work, with the aim of achieving a balance between code complexity and accuracy of the results, which is an essential feature of a DOC:

- the problem is solved in steady state, with no variable being integrated over time - a true steady state formulation is adopted, rather than, e.g., a pseudo-transient one;
- the IW channel cross section is axially constant. The entrance/exit regions located at the core bottom/top (see Fig. 1), which are part of the calculation domain, are actually characterised by an axially variable cross section. However, these regions are not directly modelled, their presence being accounted for by means of localised loss coefficients, see Section 3.2, which can be determine by means of, e.g., CFD calculations;
- energy deposition by viscous dissipation in the coolant is neglected;
- axial heat and momentum transfer via conduction and turbulent momentum flux, respectively, are neglected;
- the channel is assumed to be vertical, therefore gravity only contributes as a body force to the axial momentum balance.

In the following, the governing equations for the SC method are presented, simplified according to the above-mentioned assumptions for the problem at hand. Boundary conditions are also indicated. The resulting formulation is consistent with Chen (1984).

2.3.2. Conservation of mass

Conservation of mass describes the axial evolution of the mass flow rate in each SC, accounting for the net mass exchange with the neighbouring ones. This can be caused by either pressure differences or density differences (buoyancy effects).

The complete form of the mass conservation equation for the i-th SC reads:

$$A_i \Delta z \frac{\partial}{\partial t} \langle \rho_i \rangle + \Delta \dot{m}_i = -\Delta z \sum_{j=1}^{N_{nei,i}} W_{ij} \tag{1}$$

where Δz is the axial length of the SC - which will also be called *Control Volume* (CV) in the following. Here and thereafter, the axial variation of a quantity ψ between z (i.e., the axial coordinate of the CV inlet) and $z + \Delta z$ (i.e., the axial coordinate of the CV outlet) is expressed as $\Delta\psi = \psi_{z+\Delta z} - \psi_z$. The operator $\langle\ \rangle$ indicates volume-averaged quantities over the control volume. The subscript j denotes quantities related to one of the $N_{nei,i}$ neighbours of SC i ($N_{nei} = 2$ for *edge SCs* and $N_{nei} = 3$ for *corner SCs*). The subscript ij indicates exchange quantities between SC i and SC j. A is the cross-sectional SC flow area, ρ is the fluid density, v is the fluid velocity, $\dot{m} = \{\rho v A\}$ is the axial mass flow rate (where the $\{\ \}$ operator represents a surface average over the flow area) and W is a mass flow rate per unit length in $\mathrm{kg/(m\,s)}$. In steady state, the equation becomes:

$$\frac{\Delta \dot{m}_i}{\Delta z} = -\sum_{j=1}^{N_{nei,i}} W_{ij} \tag{2}$$

As far as boundary conditions are concerned, TIFONE receives as input the total mass flow rate to the IW region and further subdivides it radially among the SCs. The approach for doing so depends on the treatment of the transverse momentum conservation equation, as described in Section 2.3.4. The user is nevertheless left with the possibility to independently choose the flow repartition among SCs in the IW region. This capability will, for example, allow the designer to test the effectiveness of, e.g., local orificing to tune the mass flow rate in a subset of the IW SCs.

2.3.3. Conservation of energy

Conservation of energy describes the axial evolution of the coolant enthalpy in each SC, accounting for the energy deposition in the SC, the

heat transfer with the portion of the wrapper wetted by the SC and the net energy exchange with neighbouring SCs. The latter can be caused by either net mass exchange (with the consequent energy transport) or by mixing effects which do not imply a net mass exchange (conduction and turbulent mixing).

The energy conservation equation can be stated as follows:

$$A_i \Delta z \frac{\partial}{\partial t}\left[\langle \rho h \rangle_i\right] + \Delta\left[\dot{m}_i \left\{h_i\right\}\right] = A_i \Delta z \dot{q}_{eq,i} - \Delta z \sum_{j=1}^{N_{nei,i}} \left[\left\{W_{ij}^{*D} h_i\right\} - \left\{W_{ji}^{*D} h_j\right\}\right] - \Delta z \sum_{j=1}^{N_{nei,i}} W_{ij}\left\{h^{\star}\right\} + A_i \Delta z \left\langle \frac{dP_i}{dt} \right\rangle \tag{3}$$

where h is the fluid enthalpy, $\dot{q}_{eq,i}$ is the equivalent power per unit volume deposited in the SC due to either heat transfer with the adjacent SA or the volumetric heat generation, W_{ij}^{*D} and W_{ji}^{*D} are turbulent interchange flow rates per unit length between SCs, $\{h^*\}$ is an effective enthalpy transported by the cross flow (averaged over the contact area between SCs i and j) and P is the static pressure.

For the sake of simplicity, it can be assumed that $\left\{\rho h_i v\right\} \sim h_i \{\rho v\}$, where v is the flow axial velocity. Based on the axially-averaged nature of the equation, this is tantamount to assuming that h_i is representative of both the area-averaged enthalpy $\left\{h_i\right\}$ and of the volume-averaged enthalpy $\langle h_i \rangle$ for SC i. Consistently, $\left\{W_{ij}^{*D} h_i\right\} - \left\{W_{ji}^{*D} h_j\right\} \sim W_{ij}^{*D} h_i - W_{ji}^{*D} h_j$. Moreover, for single phase flow, $W_{ij}^{*D} h_i - W_{ji}^{*D} h_j = W_{ij}^{*H}\left(h_j - h_i\right)$, where W_{ij}^{*H} is the effective mass flow rate per unit length for energy exchange between SCs i and j. By applying these simplifications, the steady state energy conservation equation becomes:

$$\frac{\Delta}{\Delta z}\left(\dot{m} h_i\right) = A_i \dot{q}_{eq,i} - \sum_{j=1}^{N_{nei,i}} W_{ij}^{*H}\left(h_j - h_i\right) - \sum_{j=1}^{N_{nei,i}} W_{ij}\left\{h^*\right\} \tag{4}$$

In the IW region, the effective energy exchange between SCs i and j, $W_{ij}^{*H}\left(h_i - h_j\right)$, is in general associated to two contributions:

$$W_{ij}^{*H}\left(h_i - h_j\right) = q''_{ij} s_{ij}\Big|_{conduction} + q''_{ij} s_{ij}\Big|_{turbulence} \tag{5}$$

where q'' is a heat flux and s is the width of the gap between adjacent SCs.

The *conduction* contribution can be expressed as follows:

$$q''_{ij} s_{ij}\Big|_{conduction} = \bar{\rho}_{ij} s_{ij} \kappa_{ij} \left(\frac{\bar{\alpha}_{ij}}{\eta_{ij}}\right)\left(h_i - h_j\right) \tag{6}$$

where α is the fluid thermal diffusivity, η is the centroid-to-centroid distance between the SCs, $\kappa = \frac{\eta}{l}$ is the *conduction shape factor*, that is, the ratio between the centroid-to-centroid distance and the *effective mixing length* l. Quantities characterised by a bar ($\bar{}$) are averaged between SCs i and j. Note that, to simplify notation, here and thereafter the volume average nature of the physical quantities appearing in the equations is not explicitly stated (e.g., $\bar{\rho}_{ij} = \left(\langle \rho_i \rangle + \left\langle \rho_j \right\rangle\right)/2$ would simply be written as $\left(\rho_i + \rho_j\right)/2$).

The *turbulence* contribution can be characterised as follows:

$$q''_{ij} s_{ij}\Big|_{turbulence} = W_{ij}^{T,H}\left(h_i - h_j\right) \tag{7}$$

where $W^{T,H}$ is the effective mass exchange rate between adjacent SCs due to turbulent interchange. Chen (1984) proposed to correlate $W^{T,H}$ to the eddy diffusivity (ε) concept, thus writing:

$$W_{ij}^{T,H} = \bar{\rho}_{ij} s_{ij} \left(\frac{\varepsilon_{ij}}{\eta_{ij}}\right) \tag{8}$$

Correlations for κ_{ij} and ε_{ij} - or, alternatively, $W_{ij}^{T,H}$ - are presented in Section 3.4.

The energy source term $\dot{q}_{eq,i}$ can be characterised as follows:

$$\dot{q}_{eq,i} = \dot{q}_i + \sum_{m=1}^{N_{w,i}} \frac{q''_{w,o,m} p_{h,m}}{A_i} \tag{9}$$

where $\dot{q}_i$ is the heat deposited in the coolant per unit volume (e.g., due to gamma rays) and the second one represents the contribution of heat transfer with the wrapper. The summation runs over the number of wrapper walls in contact with the SC. $q''_{w,o,m}$ is the heat flux crossing the mth wrapper outer surface (hence the subscript o) in contact with SC i. $p_{h,m}$ is the heated perimeter associated to the m-th wall in contact with SC i.

As for boundary conditions, the inlet temperature distribution is specified by the user.

2.3.4. Conservation of momentum

Conservation of momentum describes the axial and radial evolution of the coolant momentum in each SC, accounting for the effect of gravity, friction with the portion of the wrapper wetted by the SC, localised pressure losses and net momentum exchange with neighbouring SCs. The latter can be caused by either net mass exchange (with the consequent momentum transport) or by mixing effects (which do not imply a net mass exchange). In the following, both the axial and radial momentum equations and their simplifications will be discussed.

Axial. The axial momentum conservation can be stated as follows:

$$\begin{aligned}\Delta z \frac{\partial}{\partial t}\langle \dot{m}_i \rangle + \Delta\left[\dot{m}_i \left\{v_i\right\}\right] = &-A_i \Delta z \langle \rho_i \rangle g - A_i \Delta\{P\} \\ &- \Delta z \sum_{j=1}^{N_{nei}} \left[\left\{W_{ij}^{*D} v_i\right\} - \left\{W_{ji}^{*D} v_j\right\}\right] - \Delta z \sum_{j=1}^{N_{nei}} W_{ij}\left\{v^{\star}\right\} \\ &- \Delta z \frac{1}{2}\langle \rho_i \rangle v_i^2 A_i \frac{f_i}{D_{H,i}} - A_i \Delta P_{form,i}\end{aligned} \tag{10}$$

where W_{ij}^{*D} and W_{ji}^{*D} are turbulent interchange flow rates per unit length between SCs, v^* is an effective velocity transported by the cross flow (averaged over the contact area between SCs i and j), g is the gravitational acceleration, f is the friction factor with the walls, $D_H = 4A/p_w$ is the hydraulic diameter (where p_w is the wetted perimeter), ΔP_{form} is the form (localised) pressure loss per unit length.

Consistently with the assumptions adopted in Section 2.3.3 for the energy conservation equation, for the sake of simplicity, it can be assumed that $\{\rho v v\} \sim v\{\rho v\}$, which, based on the axially-averaged nature of Eq. (10), corresponds to assuming that v_i is representative of both the area-averaged axial velocity $\left\{v_i\right\}$ and of the volume-averaged axial velocity $\langle v_i \rangle$ for SC i. Consistently, $\left\{W_{ij}^{*D} v_i\right\} - \left\{W_{ji}^{*D} v_j\right\} \sim W_{ij}^{*D} v_i - W_{ji}^{*D} v_j$. Moreover, for single phase flow, $W_{ij}^{*D} v_i - W_{ji}^{*D} v_j = W_{ij}^{*M}\left(v_j - v_i\right)$, where W_{ij}^{*M} is the effective mass flow rate per unit length for momentum exchange between SCs i and j. By applying these simplifications, the steady state axial momentum conservation equation becomes:

$$\begin{aligned}\frac{\Delta\left(\dot{m}_i v_i\right)}{\Delta z} = &-A_i \langle \rho_i \rangle g - A_i \frac{\Delta\{P\}}{\Delta z} \\ &- \sum_{j=1}^{N_{nei}} W_{ij}^{*M}\left(v_i - v_j\right) - \sum_{j=1}^{N_{nei}} W_{ij}\left\{v^*\right\} \\ &- \frac{1}{2}\langle \rho_i \rangle v_i^2 A_i \frac{f_i}{D_{H,i}} - A_i \frac{\Delta P_{form,i}}{\Delta z}\end{aligned} \tag{11}$$

The effective momentum exchange term W_{ij}^{*M}, similarly to the W_{ij}^{*H} term encountered in Eq. (4), is composed by a molecular (diffusive) contribution and a turbulent contribution which is proportional to an equivalent mass flow rate for unit length. The molecular contribution to the axial momentum exchange between SCs is usually neglected (Chen, 1984). The equivalent mass flow rate per unit length for turbulent contribution $W_{ij}^{T,M}$ is instead considered equal to its energy counterpart $W_{ij}^{T,H}$ and related to the eddy diffusivity concept. For simplicity, in the following it will be referred to simply as W_{ij}^{T}. Empirical correlations for this quantity will be discussed in Section 3.4.

As for boundary conditions, the absolute value of the inlet pressure is irrelevant, since for incompressible flow only the pressure differences

are important. Therefore, the inlet pressure can be arbitrarily specified by the user for all the SCs.

Radial. The radial momentum conservation can be generally stated as follows:

$$\frac{\partial}{\partial t}\left\langle W_{ij}\right\rangle + \frac{\Delta}{\Delta x'}\left[W_{ij}\left\{u\right\}\right] + \frac{\Delta}{\Delta z}\left[W_{ij}\left\{v\right\}\right] = -\left[s_{ij}\frac{\Delta}{\Delta x}\left\{P_j\right\}\right] - \left\{\frac{F_{ix}}{\Delta x'\Delta z}\right\} \tag{12}$$

where u is the local transverse velocity, $\Delta x'$ indicates the transverse characteristic length and F_{ix} is a force acting on the fluid along the transverse direction due to interactions with the solid. This equation is typically treated by considering a different control volume with respect to the one adopted for the foregoing equations. The control volume boundaries for the radial momentum balance can, e.g., coincide with the barycenters of the two neighbouring SCs (Todreas and Kazimi, 1990).

Solving this equation introduces significant complexity in the code structure. Moreover, the phenomenon it describes – namely, pressure-driven cross flow – is only important in the case of flow area variations and/or flow obstructions, otherwise it can be regarded as second-order effect. For the problem at hand, and in compliance with the required simplicity of a DOC, these effects can be neglected. Therefore, this equation reduces to imposing an equal pressure drop among all the SCs for each axial step:

$$P_i = P_j \quad \forall i,j \tag{13}$$

Due to this approximation, the radial distribution of the mass flow rate among SCs at the inlet section must be determined via a *flow split* model, which will be described in Section 2.4.3.

2.3.5. Heat transfer with the wrapper

TIFONE evaluates the axial distribution of the outer wrapper temperature, with a radial resolution allowing to distinguish each of the six sides of the wrapper.

The code receives as input an arbitrary (axial and radial) distribution of the heat flux crossing the wrapper outer surface, $q''_{w,o}$, which is then interpolated to compute the heat source $q''_{w,o,m}$ appearing in Eq. (9). Once $q''_{w,o,m}$ is known, the outer wrapper temperature is computed as:

$$T_{w,o,m} = T_{sc} + q''_{w,o,m}/\alpha_o \tag{14}$$

where T_{sc} is the mass flow averaged temperature of the IW coolant wetting wrapper surface m and α_o is the corresponding heat transfer coefficient. Correlations for the Nusselt number, allowing the evaluation of the heat transfer coefficient, are presented in Section 3.3.

In view of the potential interest of the designer for knowledge of the wrapper *inner* temperature distribution, the following estimate is proposed:

$$T_{w,i,m} = T_{w,o,m} + \frac{q''_{w,o,m}k_w}{s_w} \tag{15}$$

where k_w is the wrapper thermal conductivity and s_w is the wrapper thickness. This formulation neglects heat deposition in the wrapper and heat conduction between wrapper nodes, and is therefore to be regarded as a first approximation.

2.4. Solution method

A convenient solution method for SC equations in mixed convection has been proposed by Chen (1984). It was verified that this method provides good results also in the limiting case of a forced convection regime. The equations are first re-written so that the unknowns are the density and velocity variations for each SCs, as well as the axial pressure drop (which is the same among each SCs, due to the simplification of the transverse momentum equation). To achieve this result, the increments of the quantities appearing in the equations of a generic control volume i located between the axial locations z and $z+\Delta z$ are expressed as follows:

$$\begin{aligned}
&\Delta\dot{m}_i = \left(\rho_i v_i A_i\right)_{z+\Delta z} - \left(\rho_i v_i A_i\right)_z \\
&\Delta\left(\dot{m}_i h_i\right) = \left(\rho_i v_i A_i h_i\right)_{z+\Delta z} - \left(\rho_i v_i A_i h_i\right)_z \\
&\Delta\left(\dot{m}_i v_i\right) = \left(\rho_i v_i^2 A_i\right)_{z+\Delta z} - \left(\rho_i v_i^2 A_i\right)_z \\
&A_i\Delta\left\{P_i\right\} = A_i\Delta P \\
&\rho_{z+\Delta z} = \rho_z + \Delta\rho \\
&h_{z+\Delta z} = h_z + \Delta h \\
&v_{z+\Delta z} = v_z + \Delta v
\end{aligned} \tag{16}$$

Moreover, the enthalpy is eliminated in favour of the density, taking advantage of the relation $\Delta h \sim R\Delta\rho$ where $R = \left(\frac{\partial h}{\partial \rho}\right)$ can be determined by numerical differentiation of the correlations for thermophysical properties.

The form of the equations obtained by adopting these approximations and rearranging terms is discussed in the following sections.

2.4.1. Conservation of mass

The total mass balance is enforced at each axial level to close the system of equations, rather than solving the mass conservation equation for each SC:

$$\sum_{i=1}^{N_{subc}}\Delta\dot{m}_i = \sum_{i=1}^{N_{subc}} A_i\left(v_{i,z}+\Delta v_i\right)\Delta\rho_i + \sum_{i=1}^{N_{subc}} A_i\rho_{i,z}\Delta v_i = 0 \tag{17}$$

A more compact notation is the following:

$$\sum_{j=1}^{N_{subc}}\left(C_{\rho i}\Delta\rho_i + C_{vi}\Delta v_i\right) = 0 \tag{18}$$

where:

$$C_{\rho i} = A_i(v_{i,z}+\Delta v_i) \tag{19}$$

$$C_{vi} = A_i\rho_{i,z} \tag{20}$$

2.4.2. Conservation of energy

First, the term $\sum_{j=1}^{N_{nei}} W_{ij}\left\{h^*\right\}$ is approximated as $H_i^*\sum_{j=1}^{N_{nei}} W_{ij}$, where the auxiliary quantity H_i^* is rigorously defined as:

$$H_i^* = \frac{\sum_{j=1}^{N_{nei}}\left[\left|x_{ij}\right|\left(h_i+h_j\right) - x_{ij}\left(h_i-h_j\right)\right]}{2\sum_{j=1}^{N_{nei}}\left|x_{ij}\right|} \tag{21}$$

where $x_{ij} = \Delta\dot{m}_i - \Delta\dot{m}_j$, thus representing an indicator of the net mass exchange between SCs i and j occurring in the axial interval Δz. However, it has been observed that using this expression for H_i^* could hinder the code convergence (Lodi, 2017). For this reason, the option is left to use the simpler approximation $H_i^* \sim h_i$.

By further enforcing the continuity equation to be satisfied, $\frac{\Delta\dot{m}_i}{\Delta z} = -\sum_{j=1}^{N_{nei}} W_{ij}$, by exploiting equation (16) and eventually rearranging the terms, the energy equation for SC i can be written as:

$$S_i\Delta\rho_i + B_i\Delta v_i = Q_i\Delta z + EEX_i \tag{22}$$

where:

$$S_i = \left(v_{i,z}+\Delta v_i\right)\left[-H_i^* + h_{i,z} + R\left(\rho_{i,z}+\Delta\rho_i\right)\right] \tag{23}$$

$$B_i = \rho_{i,z}\left(h_{i,z} - H_i^*\right) \tag{24}$$

$$EEX_i = -\frac{\Delta z}{A_i}\sum_{j=1}^{N_{nei}}\bar{\rho}_{ij}s_{ij}\left[\kappa_{ij}\left(\frac{\bar{\alpha}_{ij}}{\eta_{ij}}\right) + \left(\frac{\epsilon_{ij}}{\eta_{ij}}\right)\right]\left(h_i - h_j\right) \tag{25}$$

2.4.3. Conservation of momentum

Axial. First, the term $\sum_{j=1}^{N_{nei}} W_{ij} \{v^*\}$ is approximated as $V_i^* \sum_{j=1}^{N_{nei}} W_{ij}$, where the auxiliary quantity V_i^* is defined by an expression analogous to equation (21):

$$V_i^* = \frac{\sum_{j=1}^{N_{nei}} \left[\left| x_{ij} \right| \left(v_i + v_j \right) - x_{ij} \left(v_i + v_j \right) \right]}{2 \sum_{j=1}^{N_{nei}} \left| x_{ij} \right|} \tag{26}$$

This expression for V_i^* could determine convergence issues which are similar in nature to those already pointed out for H_i^*. For this reason, the simpler approximation $V_i^* \sim v_i$ is also made available.

As it has been done in Section 2.4.2, by enforcing the continuity equation to be satisfied, by explicitly writing the term $\Delta \dot{m}_i$ and eventually rearranging the terms, the momentum equation for SC i can be written as:

$$E_i \Delta \rho_i + F_i \Delta v_i + \Delta P = G_i + MEX_i \tag{27}$$

where:

$$E_i = \left(v_{i,z} + \Delta v_i \right) \left(v_{i,z} + \Delta v_i - V_i^* \right) + \frac{f_i \Delta z}{16 D_{e,i}} \left(2 v_{i,z} + \Delta v_i \right)^2 + \frac{g \Delta z}{2} \tag{28}$$

$$F_i = \rho_{i,z} \left[\left(2 + \frac{f_i \Delta z}{2 D_{e,i}} \right) v_{i,z} + \left(1 + \frac{f_i \Delta z}{8 D_{e,i}} \right) \Delta v_i - V_i^* \right] \tag{29}$$

$$G_i = -\rho_{i,z} \left(g \Delta z + \frac{f_i \Delta z}{2 D_{e,i}} v_{i,z}^2 \right) \tag{30}$$

$$MEX_i = -\frac{\Delta z}{A_i} \sum_{j=1}^{N_{nei}} \bar{\rho}_{ij} s_{ij} \left(\frac{\varepsilon_{ij}}{\eta_{ij}} \right) \left(v_i - v_j \right) \tag{31}$$

Radial - flow split model. As anticipated above, in the absence of a transverse momentum equation, a flow split model is employed to estimate how the inlet flow rate in the IW region distributes among the SCs.

According to Eq. (13), the pressure drop among all the SCs is assumed to be equal. By equating the expressions for the pressure drop associated to each SC, a set of nonlinear equations is obtained having as unknowns the flow fractions for each SC i, X_i (Lodi, 2017). Starting from the difference form of Eq. (13):

$$\Delta P_i = \Delta P_j \quad \forall i, j \tag{32}$$

For incompressible flow in parallel hydraulic channels of constant cross sections, ΔP is due to head losses (both localised and distributed) and to the hydro-static pressure. The latter being approximately equal for all SCs, the equation can be written as:

$$v_i^2 \frac{f_i}{D_{H,i}} L + \xi_i v_i^2 = v_j^2 \frac{f_j}{D_{H,j}} L + \xi_j v_j^2 \tag{33}$$

where L is the total axial length of the domain and the form pressure loss term has been expressed as $\Delta P_{form} = \frac{1}{2} \rho \xi_i v_i^2$, where ξ is the sum of the localised pressure loss coefficients for SC i. The term $\frac{1}{2}\rho$ has been simplified in Eq. (33).

f, D_H and ξ are shared by SCs of the same type (i.e., having the same shape - *corner* or *side* - and the same cross section). It is therefore convenient to classify SCs among N_{cat} categories before proceeding to the solution of the flow split system, thus eliminating redundant equations. In the following, i and j will therefore indicate different SC categories.

It is customary to introduce a flow split parameter $X = \frac{v}{v_{ave}}$ where v_{ave} is the velocity averaged over all the SCs in the domain. Eq. (33) can then be written as:

$$\frac{X_i}{X_j} = \sqrt{\frac{f_j \frac{L}{D_{H,j}} + \xi_j}{f_i \frac{L}{D_{H,i}} + \xi_i}} \quad \forall i, j \tag{34}$$

These $N_{cat} - 1$ equations must be closed by relying on the continuity equation:

$$\sum_{i=1}^{N_{cat}} \frac{N_i A_i}{A_{tot}} X_i = 1 \tag{35}$$

The resulting nonlinear system of equations is solved iteratively.

2.4.4. Heat transfer in the wrapper

The wrapper temperature can be computed after having solved the problem for the coolant by simply evaluating equation (14) for each wrapper node m.

2.4.5. Matrix form of the system

The solution process involves treating one "slice", that is, one axial level, at a time. For each axial level k, the system of Eqs. (18), (22) and (27) is solved to find the increment $\Delta \rho_i$ and Δv_i for each SC, as well as the pressure drop ΔP, which has been assumed to be equal for all the SCs. The matrix form of the system of equations is the following:

$$\begin{bmatrix} S_1 & B_1 & 0 & 0 & \dots & 0 & 0 & 0 \\ E_1 & F_1 & 0 & 0 & & 0 & 0 & 1 \\ 0 & 0 & S_2 & B_2 & & 0 & 0 & 0 \\ 0 & 0 & E_2 & F_2 & & 0 & 0 & 1 \\ \vdots & & & & \ddots & & & \vdots \\ 0 & 0 & 0 & 0 & & S_{N_{subc}} & B_{N_{subc}} & 0 \\ 0 & 0 & 0 & 0 & & E_{N_{subc}} & F_{N_{subc}} & 1 \\ C_{\rho 1} & C_{v1} & C_{\rho 2} & C_{v2} & \dots & C_{\rho N_{subc}} & C_{v N_{subc}} & 0 \end{bmatrix} \begin{bmatrix} \Delta \rho_1 \\ \Delta v_1 \\ \Delta \rho_2 \\ \Delta v_2 \\ \vdots \\ \Delta \rho_{N_{subc}} \\ \Delta v_{N_{subc}} \\ \Delta P \end{bmatrix} = \begin{bmatrix} Q_1 \Delta z + EEX_1 \\ G_1 + MEX_1 \\ Q_2 \Delta z + EEX_2 \\ G_2 + MEX_2 \\ \vdots \\ Q_{N_{subc}} \Delta z + EEX_{N_{subc}} \\ G_{N_{subc}} + MEX_{N_{subc}} \\ 0 \end{bmatrix} \tag{36}$$

The solution of system (36) is necessarily iterative due to its nonlinear nature. The problem is initialised by assuming a linear temperature increase based on the total incoming power to the IW region, and computing the $\Delta \rho_i$ accordingly. The Δv_i are all considered null, whereas the ΔP is approximated to its hydrostatic value. The linear system is then solved to update the guess for $\Delta \rho_i$, Δv_i and ΔP. The solution is achieved via either the Gauss Elimination Method or the Greene method suggested in Chen (1984). The procedure is repeated up to convergence. The convergence check is posed on $\Delta \rho_i$, Δv_i and ΔP, as well as on the total mass conservation.

Once the solution for node k is available, the values of the unknowns at the beginning of node $k+1$ are computed and the procedure is repeated until all the axial nodes have been processed.

2.4.6. Coolant and wrapper temperature calculation

After having solved the system, Δh is determined from the density variation according to the relation $\Delta h \sim R \Delta \rho$, where $R = \left(\frac{\partial h}{\partial \rho} \right)$. This eventually allows to determine the temperature T_{sc} for each SC at the axial node between z and $z + \Delta z$ as $T_{sc} = T_{sc,z} + \frac{\Delta h}{2 c_p}$.

Once the coolant temperature is known, the wrapper temperature is simply computed according to Eq. (14) for each wrapper node.

3. Constitutive relations

Constitutive equations are required by TIFONE to compute friction factors f, localised pressure loss coefficients ξ, Nusselt numbers Nu (from which heat transfer coefficients α are obtained), conduction shape factors κ and eddy diffusivities ε.

Moreover, a metric for identifying the flow regime in terms of buoyancy effects is needed to understand whether the problem at hand falls within TIFONE calculation domain.

3.1. Friction factor

From the hydraulic point of view, LMs behave similarly to more common fluids such as, e.g., subcooled water (NEA, 2015), hence typically adopted empirical correlations are applicable. Such correlations are adapted to the duct geometry relevant for the present work by means of the hydraulic diameter concept: $D_h = 4A/p_w$, where p_w is the wetted perimeter of the SC, and by a corrective factor which accounts for the different shape of the SC.

3.1.1. Blasius

Blasius (1913) has proposed a simple correlation for the friction factor in a smooth circular tube:

$$f = \frac{0.316}{Re_{D_h}^{0.25}} \tag{37}$$

where $Re_{D_h} = \left(\rho v D_h\right)/\mu$ is the Reynolds number computed using the hydraulic diameter as the characteristic length. This correlation is applicable in turbulent regime up to $Re < 10^5$. No general accuracy is specified inside the validity range.

3.1.2. Colebrook/Haaland

Colebrook (1939) has proposed an empirical fit of the pipe flow pressure drop data which is valid for turbulent flow, $Re < 10^8$:

$$\frac{1}{\sqrt{f}} = -2.0 \log\left(\frac{\epsilon/D_h}{3.7} + \frac{2.51}{Re_{D_h}\sqrt{f}}\right) \tag{38}$$

where ϵ represents the surface roughness. An accuracy of $\sim 15\%$ can be expected from using this formula for a noncircular duct applying the hydraulic diameter concept.

Haaland (1983) has proposed a formula approximating the Colebrook/Moody chart which is explicit in f:

$$\frac{1}{\sqrt{f}} = -1.8 \log\left(\left(\frac{\epsilon/D_h}{3.7}\right)^{1.11} + \frac{6.9}{Re}\right) \tag{39}$$

3.1.3. Liang

An experimental setup consisting of three converging gaps and using deionised water as a working fluid has been employed by Liang et al. (2021) to validate a numerical model both in laminar and in turbulent conditions. The validated numerical model has then been adopted to extrapolate the friction factor correlations to other values of the channel aspect ratio β.

The recommended correlation for the friction factor in the IW region in laminar flow regime ($Re < 2500$) is the following:

$$f \cdot Re = C_l \tag{40}$$

where:

$$C_l = 96\left(1 + 0.2149\beta + 0.01572\beta^2 - 0.0256\beta^3 + 0.02413\beta^4 - 0.008649\beta^5\right) \tag{41}$$

The authors of this study recommended that the correlation proposed by Sadatomi is used for the turbulent flow regime ($Re > 3200$) (Sadatomi et al., 1982) :

$$f = \frac{C_t}{Re^{0.25}} \tag{42}$$

where C_t is a geometry factor for turbulent flow, which is computed as:

$$\frac{C_t}{C_{t,0}} = \sqrt[3]{0.0154\frac{C_l}{C_{l,0}} - 0.012} + 0.85 \tag{43}$$

where $C_{t,0} = 0.3164$ and $C_{l,0} = 64$ are the constants for circular pipe in laminar and turbulent regime, respectively, and C_l can be computed by means of Eqs. (40) and (41).

3.1.4. Corrective factor for non-circular geometries

To any of the above correlations that is selected to represent a reference circular duct, a corrective factor is to be introduced to account for the actual, non-circular shape of the considered SC. For this, according to the Idelchik handbook (Idelchik, 2007), depending on the case-specific conditions, a corrective factor $k_{\text{non-c}}$ can be introduced to finally obtain the distributed pressure drops.

For laminar flow ($Re < 2000$) in rectangular channels the correction factor lies in the range $0.89 < k_{\text{non-c,lam}} < 1.5$, the specific value depending on the aspect ratio of the channel. The limit for a plane slot ($a/b \to 0$), which is the relevant geometry for *edge SCs*, is $k_{\text{non-c,lam,edge}} = 1.5$.

For turbulent flow ($Re > 2000$) in rectangular channels the correction factor lies in the range $1.0 < k_{\text{non-c,turb}} < 1.1$, with the specific value depending again on the aspect ratio of the channel. The limit for a plane slot ($a/b \to 0$), is $k_{\text{non-c,turb,edge}} = 1.1$.

3.2. Localised pressure loss coefficient

Due to the assumption concerning the geometry of the channel, the only localised pressure losses are associated to the inlet and outlet sections (see Fig. 1). The associated pressure loss coefficients – falling outside the scope of TIFONE – are therefore specified by the user, so that the input file and associated reader can include means to provide such information.

3.3. Nusselt number

To what concerns correlations for the Nusselt number, the literature review performed in the latest edition of the NEA liquid metal handbook (NEA, 2015) is here followed.

3.3.1. Kays

The correlation by Kays and Leung (1963) is the only one available for nonuniform heating at the two sides of a rectangular channel:

$$Nu\Big|_{q_w=constant} = \frac{Nu_0}{1 - \gamma\varphi} \tag{44}$$

where γ is a tabulated correction factor and φ is the heat flux ratio between the two sides of the duct. Values for Nu_0, γ and φ as a function of Re and Pr are provided in Table 1 of Kays and Leung (1963). The correlation is claimed to be valid for $10^4 < Re < 10^6$ and $0 < Pr < 1000$.

3.3.2. Duchatelle

The correlation provided by Duchatelle and Vautrey (1964) has been developed for the specific case of a duct with one heated side and one adiabatic side. This physical situation is anticipated to occur only for peripheral SCs.

$$Nu = 5.85 + 0.00341\,Pe^{1.29} \tag{45}$$

The correlation is claimed to be valid for $0 \le Pr \le 0.04$ and $10^4 \le Re \le 10^5$.

3.3.3. Dwyer

The correlation proposed by Dwyer (1965), similarly to the one proposed by Duchatelle, has been developed for the specific case of a duct with one heated side and one adiabatic side.

$$Nu = 5.60 + 0.01905\,Pe^{0.775} \tag{46}$$

The correlation is claimed to be valid for $0 \le Pr \le 0.04$ and $10^4 \le Re \le 10^5$.

3.3.4. Sleicher/Rouse

In Kawamura et al. (1998), it has been shown that the correlation proposed by Sleicher and Rouse (1975) agrees well with Direct Numerical Simulation (DNS) results for the case of uniform heating. The proposed correlation is the following:

$$Nu = 6.3 + 0.0167 Re^{0.85} Pr^{0.93} \tag{47}$$

which is claimed to be valid for $0.004 < Pr < 0.1$ and $10^4 < Re < 10^6$.

3.4. Internodal mixing

No correlations for the empirical parameters describing the inter-SC mixing have been found in the literature for the specific geometry here considered. Due to this limitation, simplifying assumptions are proposed to be adopted in the current version of TIFONE, which are discussed in the following.

3.4.1. Conduction shape factor

The conduction shape factor κ appearing in the term EEX of Eq. (25) is taken equal to one (1.0) for each couple of SCs, due to the lack of better information. This is believed to represent a reasonable approximation for the energy exchange between *edge SCs* due to their simple geometry. This assumption might instead be questionable for the energy exchange between an *edge SC* and a *corner SC*.

3.4.2. Eddy diffusivity

No correlation for the eddy diffusivity ε_{ij} has been found in the literature for the particular SC geometry relevant for TIFONE. Therefore, the eddy diffusivity is put to zero (0.0) (i.e., the internodal energy exchange is assumed to be purely conductive). This approach was adopted also in Basehore and Todreas (1980) for the IW region.

3.5. Criterion for mixed convection

The TIFONE application domain encompasses both the forced and the mixed convection regimes. For this reason, a figure of merit for assessing the relevance of buoyancy effects is needed. Jackson (1983) proposed to use $Y_{mix} = \frac{Gr}{Re^2}$, and for the case of sodium flowing inside a vertical pipe the following inequality was proposed for the onset of buoyancy effects:

$$Y_{mix} > 0.002 \tag{48}$$

This value marks the transition between the forced and mixed convection regimes (an internal boundary within the TIFONE validity domain) whereas it is more difficult to characterise *a priori* the limiting value of Y_{mix} for the onset of free convection effects. In this respect, the comparison with experimental data presented in the following section offers an opportunity to *a posteriori* determine this upper bound.

4. Preliminary validation

In this section, the application of TIFONE to the simulation of recently performed IW flow and heat transfer experiments performed in the frame of the SESAME project at the THESYS loop within the KALLA laboratory is presented, together with the comparison with available measurements.

4.1. Experimental setup

During the experimental campaign here considered, detailed thermal measurements for the IW flow and heat transfer in the gap between three electrically heated SA simulators cooled by Lead–Bismuth Eutectic (LBE) were obtained. The experimental record is reported in a SESAME project deliverable (Pacio et al., 2018) and selected results are contained in a related paper (Pacio et al., 2019). A schematic of the test section cross-section is shown in Fig. 3. The three assemblies are named A, B and C, respectively, and each gap is referred to by the names of the neighbouring SAs (AB, BC, AC).

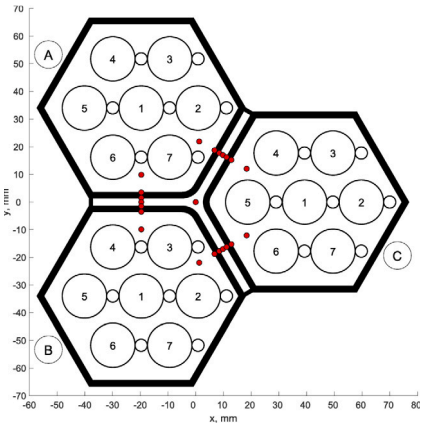

Fig. 3. Thermo-couple location for each measurement level.
Source: Reproduced from Pacio et al. (2019) with permission.

Table 1
Main geometrical parameters of the IW flow test section (Pacio et al., 2018).

Quantity	Unit	Value	Meaning
Outer dimensions			
FF	mm	65.00	Outer flat-to-flat distance
w	mm	2.0	Wall thickness
δ	mm	3.0	Gap width
Bundle dimensions			
D	mm	16.0	Rod diameter
L_{heat}	mm	600.0	Rod heated length
L_{tot}	mm	1400.0	Rod total length
P	mm	20.50	Rod pitch
W	mm	20.75	Wall distance
Flow areas			
A_{bdl}	mm^2	1704.2	Bundle channels (A–C)
A_{gap}	mm^2	331.9	Gap channel (D)
Hydraulic diameters			
$d_{h,bdl}$	mm	10.31	Bundle channels (A–C)
$d_{h,gap}$	mm	5.85	Gap channel (D)

The main geometrical parameters of the test section are reported in Table 1. The rationale for choosing these parameters is based on a scaling of the MYRRHA SA design and is described in Pacio et al. (2019).

The available measurements include:

- radial temperature distribution at two selected axial locations ($z = 393$ mm and $z = 524$ mm) with the sensor layout indicated in Fig. 3;
- axial temperature distribution at four radial locations, corresponding to the centre of the IW region and to the barycentre of each gap, respectively;
- local velocity and temperature profiles at the outlet section of gap AB;
- radial temperature distribution at the outlet of the test section along the gaps AB and BC.

4.2. TIFONE simulation setup

TIFONE simulations were prepared accounting for the test section geometry and materials, adopting the measured inlet temperature and mass flow rates as boundary conditions and imposing an arbitrary inlet pressure — which does not affect the result. Since the calculation

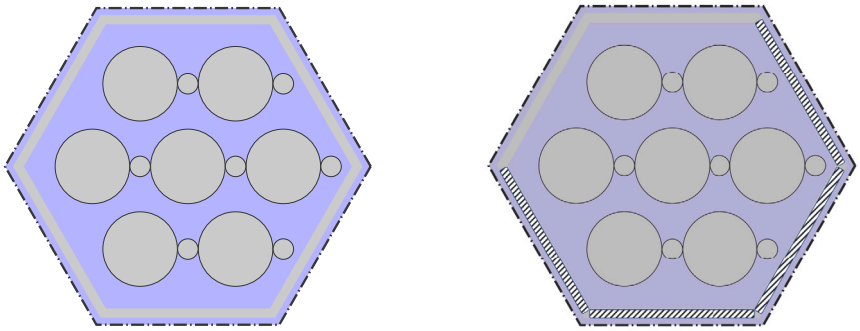

Fig. 4. Typical ANTEO+ simulation setup (left) and specific ANTEO+ simulation setup adopted in this study for each SA (right).

Table 2
TIFONE input data for symmetric validation cases.

Quantity	Unit	Case 1	Case 4	Case 6	Case 8
$\dot{m}_{ABC}$ - Mass flow rate in each SA	kg/s	3.55	3.55	3.55	3.55
$\dot{m}_{IW}$ - IW mass flow rate	kg/s	0.686	0.517	0.342	0.170
q_{ABC} - Power generated in each SA	kW	30.0	30.0	30.0	30.0
q_{IW} - Total power to IW flow	kW	3.700	3.010	2.160	1.170
q'' - Surface heat flux	kW/m^2		ANTEO+		
T_{in} - Inlet LBE temperature	°C	199.25	199.20	199.10	199.10

domain of TIFONE is limited to the inter-wrapper region, a necessary input is the distribution of the heat flux crossing the wrapper external surfaces, $q''(s,z)$, where s is a curvilinear coordinate along the wrapper external face. Since the available measurements were not sufficient to perform a reliable reconstruction of the profile, $q''(s,z)$ was estimated by means of three standalone ANTEO+ simulations, one for each SA. The resulting $q''(s,z)$ was then interpolated to yield $q''_{w,o,m}$ (see Eq. (9)), which is used to compute the equivalent heat source term $\dot{q}_{eq,i}$ appearing in the TIFONE energy equation (4).

The current version of ANTEO+ assumes that each wrapper face is cooled by the IW flow, see Fig. 4 (left). Moreover, IW heat transfer is completely neglected (the dash-dotted line in Fig. 4 (left) is an adiabatic boundary). This results in a simulation setup which is not fully representative for the physical case at hand. For this reason, an *ad-hoc* modification of ANTEO+ was performed, resulting in the setup schematised in Fig. 4 (right), which more closely represents the experimental setup, accounting for four adiabatic sides of the wrapper.

The computed axial heat flux distribution for each face was passed to TIFONE, after having been rescaled to match the total measured heat transfer to the IW coolant, if available. A couple of remarks should be made concerning this approach to estimate the heat flux across the wrapper. First, local effects such as spatially periodic temperature variations associated to the presence of the wire could not be accounted for. Second, a self-consistent coupling of TIFONE to SA codes such as ANTEO+ itself was not yet implemented at the time of writing this article but is foreseen in perspective to achieve a full-core TH solution.

As far as constitutive relations are concerned, for all the simulations presented thereafter the "default" TIFONE settings have been employed. This implies using the friction factor correlations recommended by Liang for both laminar and turbulent conditions, with the exception of corner SCs in turbulent conditions, for which the Haaland correlation was employed. For the Nusselt number, the correlation by Sleicher and Rouse was adopted.

4.3. Symmetric cases

Symmetric experimental cases are characterised by a uniform power input to the three SAs. In this section, four of these cases, labelled as 1, 4, 6 and 8 in Pacio et al. (2018), are considered. These cases are characterised by a progressive reduction in the IW flow rate, in turn resulting in reduced heat losses from the SAs, see Table 2.

Fig. 5 (left) shows the computed and measured axial profiles of the normalised SC temperature increase $\Delta\widetilde{T}$ along the corner SC. $\Delta\widetilde{T}$ is defined as:

$$\Delta\widetilde{T} = \frac{T - \overline{T}_{inlet}}{\overline{T}_{outlet} - \overline{T}_{inlet}} \tag{49}$$

where T is either the measured local temperature or the computed SC-averaged temperature, whereas $\overline{T}_{inlet}$ and $\overline{T}_{outlet}$ represent the average inlet and outlet temperatures to the test section, respectively. Comparison with experimental data points shows a good agreement, suggesting that the axial shape of the heat flux crossing the wrapper is well reproduced. Nonetheless, a discrepancy towards the top of the channel for the corner SC can be noticed, which will be further investigated in the following.

Fig. 5 (right) shows the computed and measured axial profiles of $\Delta\widetilde{T}$ at radial locations placed at the half length of each side. The computed values are very similar among the three wings due to the almost symmetric BCs provided by the three ANTEO+ simulations (see again Table 2). The measured temperature increases show instead some asymmetries, which are likely due to local effects associated e.g., to the presence of the wire.

Fig. 6 (left) shows the comparison between the computed and measured profiles of the normalised temperature increase at the outlet section. Finely sampled profiles were only available along gap AB. As for the other gaps, only three points per gap were sampled. The comparison between the computed and measured temperature increases shows a very good agreement, the largest discrepancies being at the gap centre (as it was already noticed in Fig. 5) and at the gap end.

Fig. 6 (right) shows instead the comparison between the computed and measured profiles at the outlet section for the normalised velocity $\widetilde{v}$, defined as:

$$\widetilde{v} = \frac{v}{\overline{v}_{outlet}} \tag{50}$$

where v is either the measured local axial velocity or the computed SC-averaged axial velocity, and $\overline{v}_{outlet}$ is the average velocity at the outlet of the test section. The measured velocities appear to be always larger than the computed ones. This is likely caused by the local nature of the velocity measurements, catching the value at the gap centreline, whereas TIFONE computes an average SC velocity. Accounting for this intrinsic offset, it can be stated that TIFONE overestimates the local velocity for the corner SC and underestimates it for the end of the

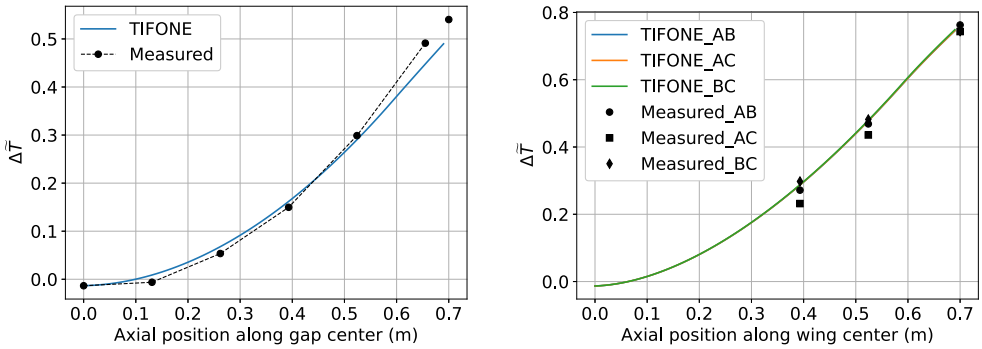

Fig. 5. Computed and measured axial evolution of the normalised temperature increase at the centre of the IW region (left) and at the centre of each gap (right) for Case 1.

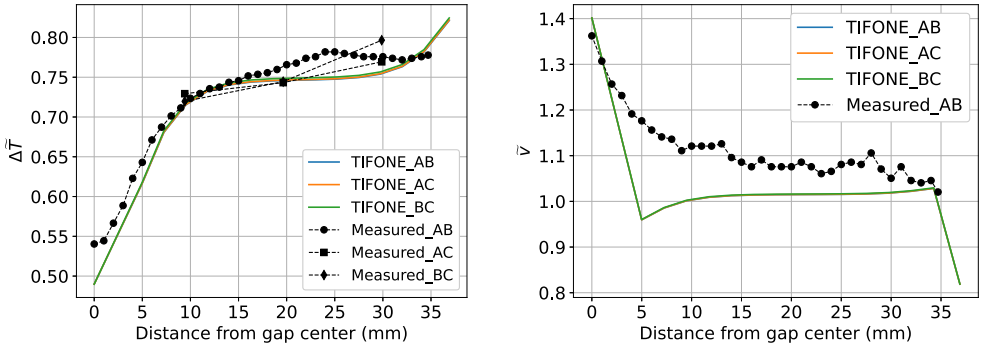

Fig. 6. Computed and measured profiles of the normalised temperature increase (left) and of the normalised velocity (right) at gap outlet for case 1.

gap, causing the above described deviations of the computed profile of the normalised temperature increase with respect to the measured one. It can also be noticed that the cusp computed at 5 mm from the gap centre is a nonphysical behaviour following from having neglected the inter-SC friction. These results suggest that, while the presented results are promising, a better treatment of both friction factor for the non-edge SCs and of inter-SC momentum exchange will be beneficial for the accuracy of the TIFONE calculation. These improvements may rely on experiments or detailed calculations to derive correlations for the eddy diffusivity in the considered gap geometry.

As mentioned in the introduction, one of the main requirements for TIFONE is the accurate calculation of the possibly different temperature distributions at each side of the wrapper. In this respect, to provide a preliminary qualification of the capabilities of the proposed approach involving ANTEO+ and TIFONE, the simulation results were compared to temperature measurements available at the radial locations indicated in Fig. 3 for two distinct axial levels (at $z = 393$ mm and $z = 524$ mm, respectively). The results of this comparison for case 1 are shown in Fig. 7 (left) and Fig. 7 (right) for the lower and upper measurement level, respectively. As for the simulation results reported in the figure, the first and last radial points (which are located inside the hexagonal assemblies) refer to ANTEO+ results, whereas the others refer to TIFONE results. Again, computed values are very similar among the three wings due to the almost identical BCs adopted for ANTEO+, which translates in almost identical BCs for TIFONE. The measured values show instead noticeable asymmetries, likely associated to local effects such as the presence of the wire which cannot be reproduced by codes based on the SC method. Having taken this intrinsic limitation into account, it can be stated that the code is capable of retrieving the basic physical feature of the solution, resulting in qualitative agreement with experimental data.

For the three further symmetric cases, as for case 1, the axial evolution of the normalised temperature increase is well reproduced, see Figs. 8 and 9, apart from the above-mentioned deviation close to the top of the test section, which is again found in case 4. Fig. 10 also shows a very good agreement on the normalised temperature increase profile along the AB gap for cases 4 and 6. For case 8, instead, the agreement is significantly worse. This can be explained in terms of the lower flow rate, implying that buoyancy effects play a dominant role, so that the mixed convection assumption is no longer valid, thus falling outside the anticipated TIFONE application domain.

As mentioned in Section 3.5, the availability of experimental data represents an opportunity to quantitatively estimate the upper bound of the validity range for the mixed convection model implemented in TIFONE in terms of Y_{mix}. To this purpose, here and thereafter, each case is characterised in terms of the maximum computed $\widetilde{Y}_{mix}$, that is, the maximum computed Y_{mix} normalised with respect to the value corresponding to the onset of mixed convection effects, $Y^*_{mix} = 0.002$:

$$\widetilde{Y}_{mix} = \frac{Y_{mix}}{Y^*_{mix}} = \frac{Y_{mix}}{0.002} \tag{51}$$

Evaluating $\widetilde{Y}_{mix}$ for the cases 1, 4, 6 and 8 yielded 0.95, 1.4, 2.5 and 13, respectively.

4.4. Asymmetric cases with $\dot{m}_C$ reduced by 20%

The first set of asymmetric cases here considered was obtained by reducing the flowrate in assembly C by 20% with respect to the cases described above, and then performing the same progressive reduction in the IW flow rate. The cases were labelled as 42, 45, 48 and 51, respectively, in Pacio et al. (2018). The resulting experimental parameters are summarised in Table 3.

The asymmetric setup results in non-negligible inter-SA heat transfer, which would require, in principle, an actual coupling of TIFONE with ANTEO+ (not implemented here).

Considering case 42 first, Fig. 11 shows that the axial evolution of the normalised temperature increase along the corner SC appears to be correctly retrieved. The radial profile at the outlet is also in satisfactory agreement with experimental data, see Fig. 12 (left). In both cases, the code correctly reproduces the different behaviour of the AB gap (which

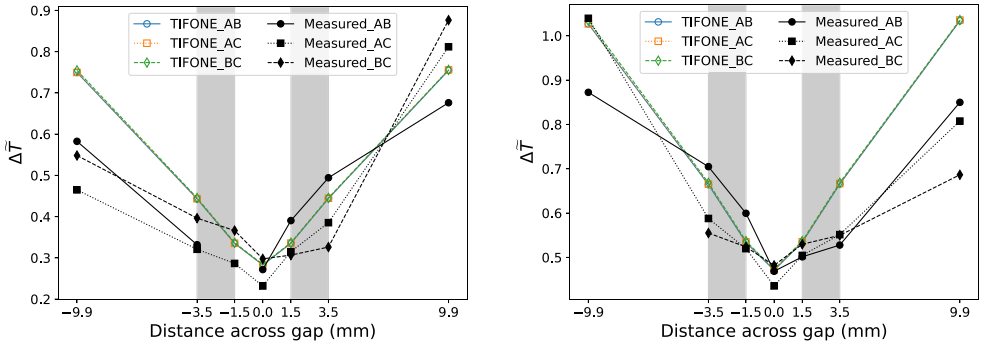

Fig. 7. Computed and measured radial distributions of the normalised temperature increase around the gap region at axial locations 393 mm (left) and 524 mm (right), for case 1. The shaded grey area indicates the radial extension of the wrapper.

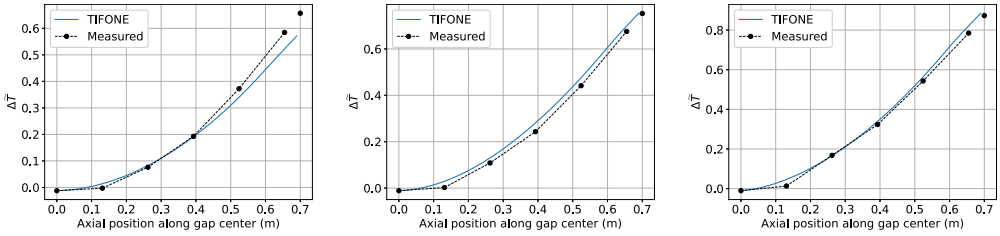

Fig. 8. Computed and measured axial evolution of the normalised temperature increase at the centre of the IW region for cases 4 (left), 6 (centre) and 8 (right).

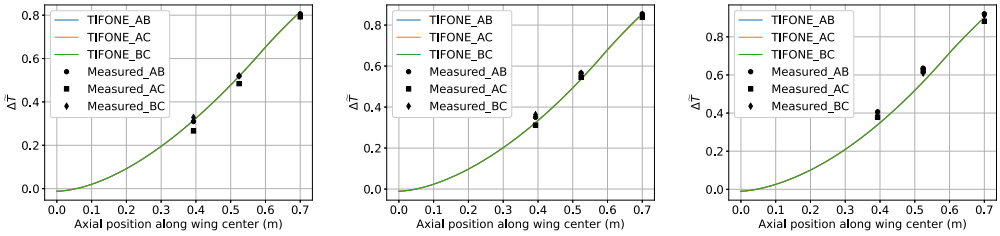

Fig. 9. Computed and measured axial evolution of the normalised temperature increase at the centre of each gap for cases 4 (left), 6 (centre) and 8 (right).

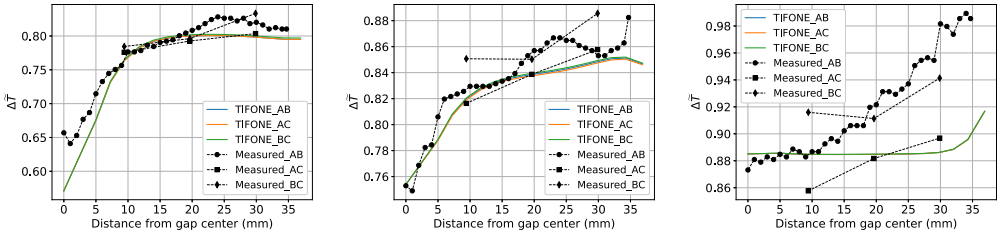

Fig. 10. Computed and measured profiles of the normalised temperature increase at gap outlet for cases 4 (left), 6 (centre) and 8 (right).

Table 3
TIFONE input data for validation cases with 20% reduction of the flowrate in assembly C.

Quantity	Unit	Case 42	Case 45	Case 48	Case 51
$\dot{m}_{AB}$ - A and B mass flow rate	kg/s	3.55	3.55	3.55	3.55
$\dot{m}_{C}$ - C mass flow rate	kg/s	2.86	2.86	2.86	2.86
$\dot{m}_{IW}$ - IW mass flow rate	kg/s	0.686	0.517	0.342	0.170
q_{ABC} - Power generated in each SA	kW	30.0	30.0	30.0	30.0
q_{IW} - Total power to IW flow	kW	4.000	3.260	2.340	1.270
q'' - Surface heat flux	kW/m^2		ANTEO+		
T_{in} - Inlet LBE temperature	°C	199.25	199.20	199.10	199.10

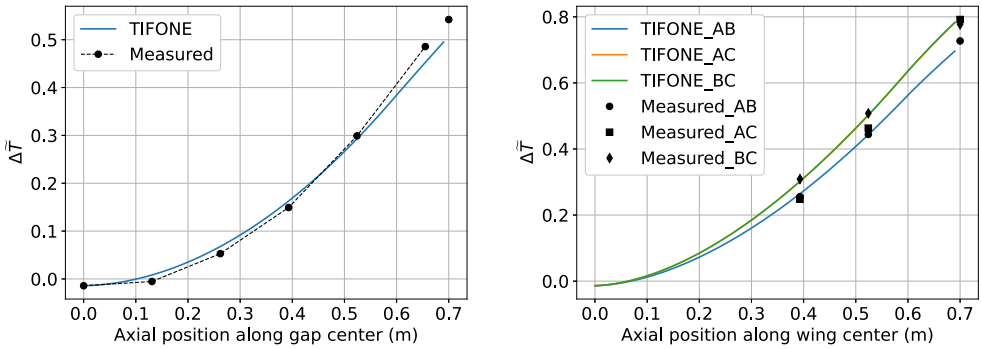

Fig. 11. Computed and measured axial evolution of the normalised temperature increase at the centre of the IW region (left) and at the centre of each gap (right) for Case 42.

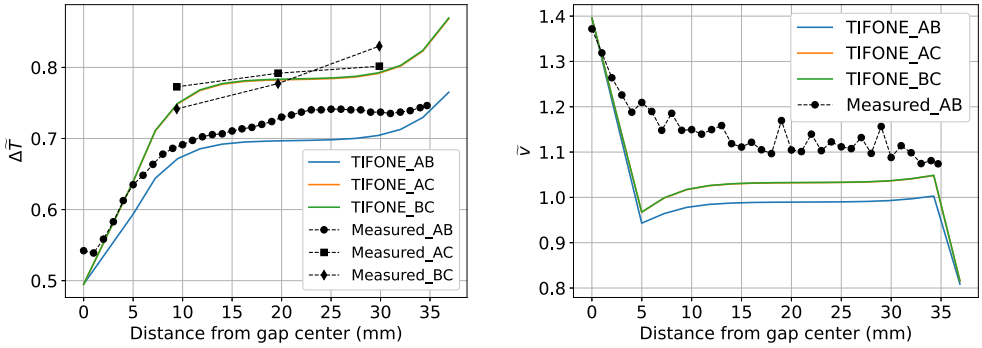

Fig. 12. Computed and measured profiles of the normalised temperature increase (left) and of the normalised velocity (right) at gap outlet for case 42.

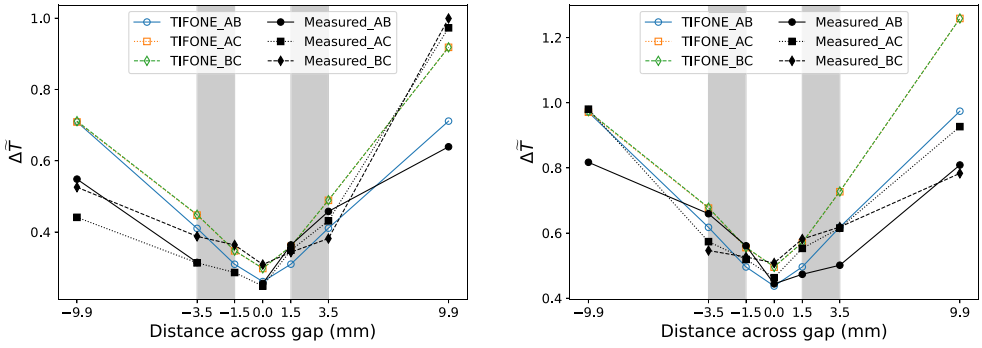

Fig. 13. Computed and measured radial distributions of the normalised temperature increase around the gap region at axial locations 393 mm (left) and 524 mm (right), for case 42. The shaded grey area indicates the radial extension of the wrapper.

is relatively unaffected by the different behaviour of assembly C) with respect to the others. These results provide further evidence of the fact that, in a mixed convection situation ($\widetilde{Y}_{mix}$ = 1.2), TIFONE correctly reproduces the measured temperature. As for the radial profile of the normalised velocity, a similar behaviour with respect to the symmetric cases is retrieved, see Fig. 12 (right).

Fig. 13 shows that the qualitative features of this asymmetric case in terms of temperatures near the gap, including the different behaviour of gap AB with respect to AC and BC, are retrieved. Nevertheless, in this case it is difficult to disentangle the discrepancies associated to the fact that the effect of the wire is here neglected from those arising from the lack of self-consistent coupling of neighbouring assemblies. This shall be the subject of future work.

Similarly to the symmetric cases above, for the three further cases considered the progressive reduction in the IW coolant flow rate results in reduced heat losses from the SAs. The axial evolution of the normalised temperature increase is still reasonably well reproduced for all cases, see Figs. 14 and 15. Fig. 16 also shows a good agreement along the AB gap for case 45 ($\widetilde{Y}_{mix}$ = 1.8). For case 48 ($\widetilde{Y}_{mix}$ = 2.8) the agreement worsens, with some features of the temperature field which are missed by the code. For case 51 ($\widetilde{Y}_{mix}$ = 16), similarly to case 4 above, buoyancy effects play a dominant role, leading to a bad agreement of the computed and measured temperatures. These results point out that a physical situation with $\widetilde{Y}_{mix}$ = 2.8 is already slightly above the mixed convection domain upper bound.

4.5. Asymmetric cases with $\dot{m}_C$ reduced by 40%

The second set of asymmetric cases here considered was obtained by further reducing the flowrate in assembly C to a value 40% lower with respect to the symmetric cases, and then performing the same progressive reduction in the IW flow rate. These cases were labelled as 55, 57, 59 and 61 in Pacio et al. (2018). Table 4 summarises the parameters adopted for these cases. The asterisk (*) indicates that calorimetric measurements for the total power deposited in the IW region were unavailable, therefore the table reports the result of

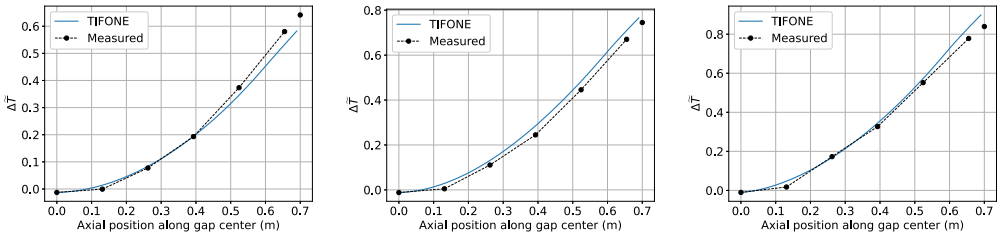

Fig. 14. Computed and measured axial evolution of the normalised temperature increase at the centre of the IW region for cases 45 (left), 48 (centre) and 51 (right).

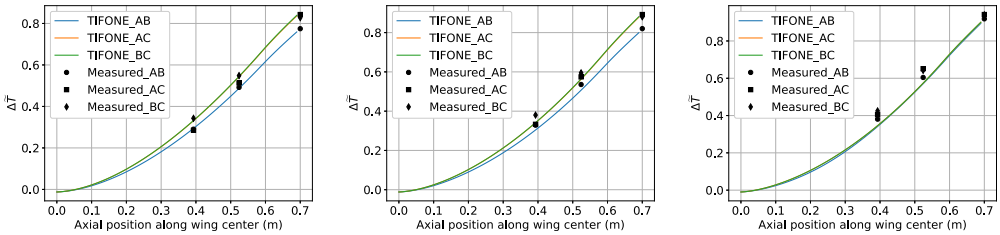

Fig. 15. Computed and measured axial evolution of the normalised temperature increase at the centre of each gap for cases 45 (left), 48 (centre) and 51 (right).

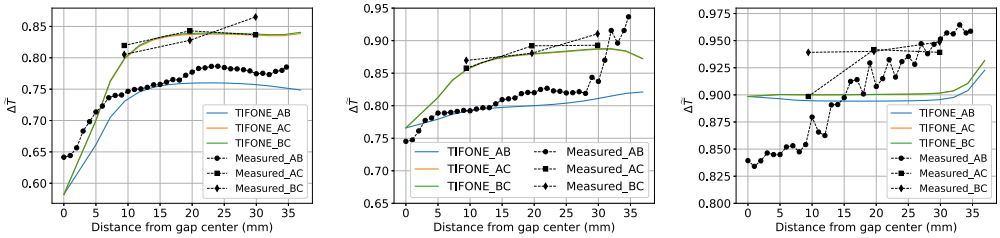

Fig. 16. Computed and measured profiles of the normalised temperature increase at gap outlet for cases 45 (left), 48 (centre) and 51 (right).

Table 4
TIFONE input data for validation cases with 40% reduction of the flowrate in assembly C.

Quantity	Unit	Case 55	Case 57	Case 59	Case 61
$\dot{m}_{AB}$ - A and B mass flow rate	kg/s	3.6	3.6	3.6	3.6
$\dot{m}_{C}$ - C mass flow rate	kg/s	2.21	2.15	2.15	2.15
$\dot{m}_{IW}$ - IW mass flow rate	kg/s	0.686	0.517	0.342	0.170
q_{ABC} - Power generated in each SA	kW	30.0	30.0	30.0	30.0
q_{IW} - Total power to IW flow (*)	kW	4.629	3.660	2.650	1.420
q'' - Surface heat flux	kW/m^2		ANTEO+		
T_{in} - Inlet LBE temperature	°C	199.1	199.1	199.0	199.0

ANTEO+ calculation, which was directly used as an input for TIFONE without any rescaling. The total power to IW flow is generally larger with respect to the 20% reduction case, since LBE in bundle C reaches larger temperatures.

Considering case 55 first, Fig. 17 shows that the axial evolution of the normalised temperature increase along the corner SC is again correctly retrieved. The radial profile at the outlet is also in satisfactory agreement with experimental data, see Fig. 18 (left), with the code correctly reproducing the different behaviour of the AB gap (which is relatively unaffected by the different behaviour of assembly C) with respect to the others. This satisfactory behaviour was expected due to the relatively low $\widetilde{Y}_{mix} = 1.7$. As for the radial profile of the normalised velocity, a similar behaviour with respect to the previously presented cases is again retrieved, see Fig. 18 (right).

Fig. 19 shows that, as for the previous asymmetric case, the computed and measured temperatures across the gap are in qualitative agreement, with the simulations correctly retrieving the different behaviour observed along gap AB with respect to gaps AC and BC, as well as the larger temperature inside assembly C.

The three further cases here considered, characterised by a progressive reduction in the IW coolant flow rate, all show a well reproduced axial profile of the normalised temperature increase, see Figs. 20 and 21. Fig. 22 also shows a very good agreement on the profile of the normalised temperature increase along the AB gap for case 57 ($\widetilde{Y}_{mix} = 2.4$). For case 59 ($\widetilde{Y}_{mix} = 3.8$) the agreement worsens, with some features of the temperature field which are missed by the code. For case 61 ($\widetilde{Y}_{mix} = 20$) buoyancy effects play a dominant role, leading to a breakdown of the mixed convection assumption with a consequent bad agreement of the computed profiles with respect to the measured ones.

4.6. Asymmetric cases with unheated bundle C

The last set of experimental cases considered in this paper was obtained by leaving bundle C unheated, and then performing the same progressive reduction in the IW flow rate. The resulting cases were labelled 32, 34, 36 and 38, respectively, in Pacio et al. (2018). Table 5 summarises the parameters adopted for these cases.

Considering case 32 first, Fig. 23 shows that the axial evolution of the normalised temperature increase along the centreline of each gap appears to be correctly retrieved, whereas for the gap centre a larger discrepancy with respect to the previous cases can be found, mainly due to the already commented overestimation of the corner SC

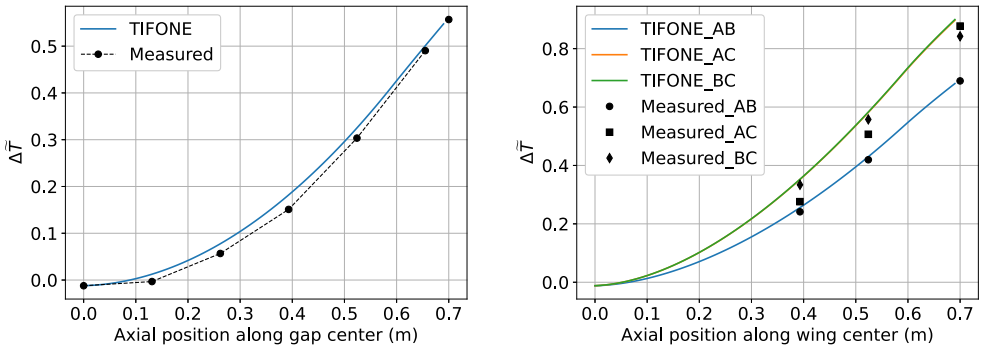

Fig. 17. Computed and measured axial evolution of the normalised temperature increase at the centre of the IW region (left) and at the centre of each gap (right) for Case 55.

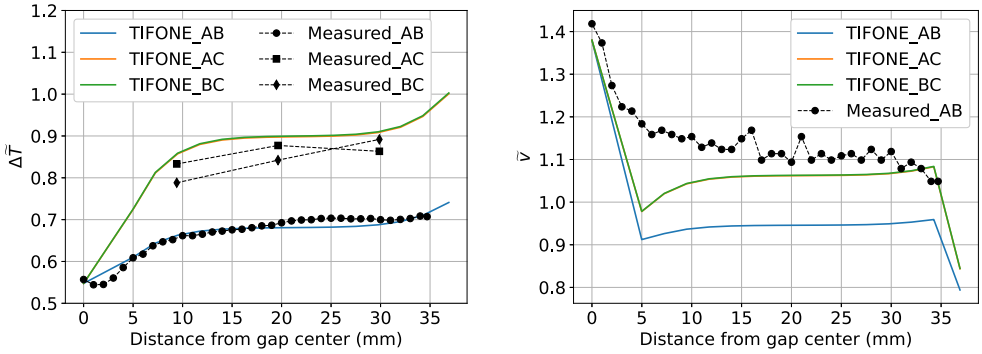

Fig. 18. Computed and measured profiles of the normalised temperature increase (left) and of the normalised velocity (right) at gap outlet for case 55.

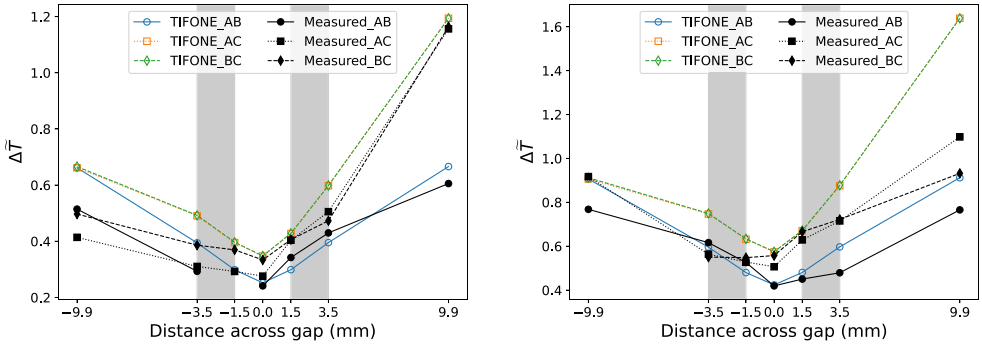

Fig. 19. Computed and measured radial distributions of the normalised temperature increase around the gap region at axial locations 393 mm (left) and 524 mm (right), for case 55. The shaded grey area indicates the radial extension of the wrapper.

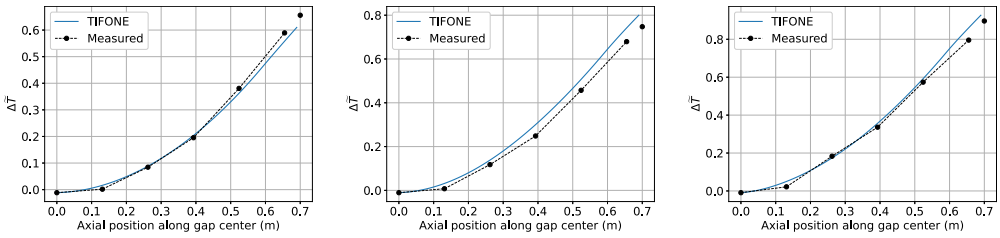

Fig. 20. Computed and measured axial evolution of the normalised temperature increase at the centre of the IW region for cases 57 (left), 59 (centre) and 61 (right).

velocity. On top of that, this case is more severely affected by the lack of self-consistent coupling between ANTEO+ and TIFONE.

The radial profile of the normalised temperature increase at the outlet is also in good agreement with experimental data, see Fig. 24 (left), apart from an offset which was traced back to the lack of self-consistent coupling rather than to buoyancy effects which should here be under control ($\widetilde{Y}_{mix}$ = 0.90). As for the radial profile of the normalised velocity, a behaviour similar to the previously analysed cases is retrieved, see Fig. 24 (right).

Fig. 25 shows that even in the most challenging situation for ANTEO+/TIFONE among those considered in this paper, characterised by the unavailability of calorimetric measurements and by strong asymmetries between assembly C and the others, a good qualitative agreement is retrieved between the computed and measured values of the

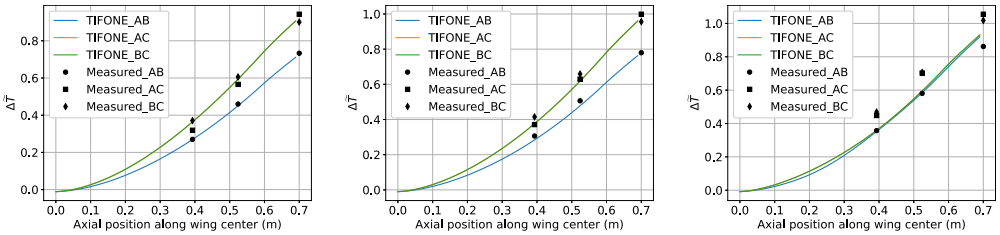

Fig. 21. Computed and measured axial evolution of the normalised temperature increase at the centre of each gap for cases 57 (left), 59 (centre) and 61 (right).

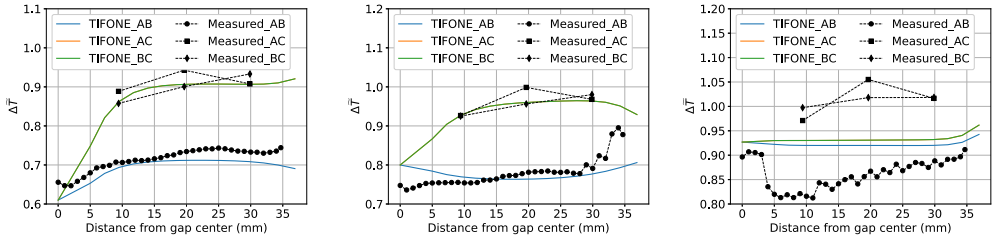

Fig. 22. Computed and measured profiles of the normalised temperature increase at gap outlet for cases 57 (left), 59 (centre) and 61 (right).

Table 5
TIFONE input data for asymmetric validation cases with unheated bundle C.

Quantity	Unit	Case 32	Case 34	Case 36	Case 38
$\dot{m}_{AB}$ - A and B mass flow rate	kg/s	3.6	3.6	3.6	3.6
$\dot{m}_{C}$ - C mass flow rate	kg/s	2.86	2.86	2.86	2.86
$\dot{m}_{IW}$ - IW mass flow rate	kg/s	0.69	0.52	0.34	0.17
q_{AB} - Power generated in each SA	kW	30.0	30.0	30.0	30.0
q_{IW} - Total power to IW flow(*)	kW	2.254	1.849	1.342	0.757
q'' - Surface heat flux	kW/m^2		ANTEO+		
T_{in} - Inlet LBE temperature	°C	199.2	199.1	199.1	199.0

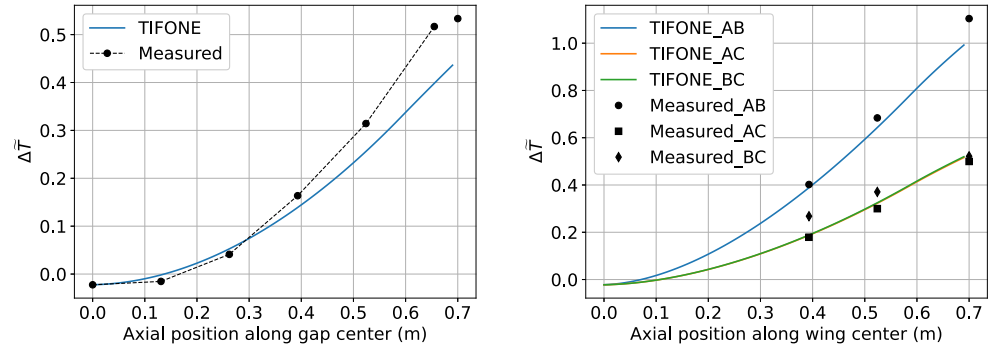

Fig. 23. Computed and measured axial evolution of the normalised temperature increase at the centre of the IW region (left) and at the centre of each gap (right) for Case 32.

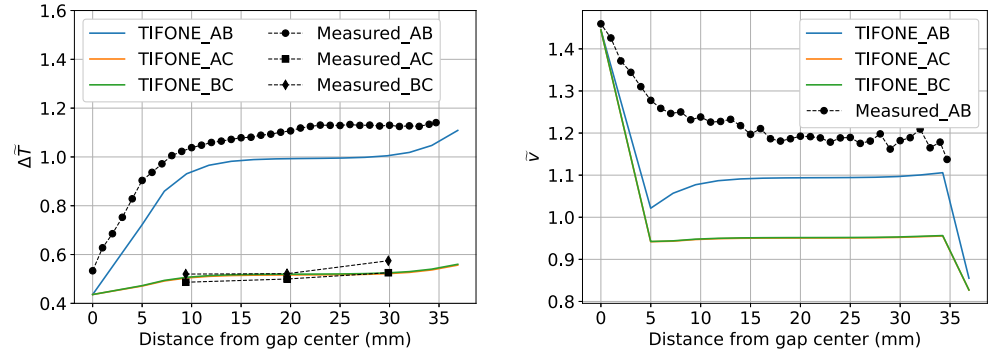

Fig. 24. Computed and measured profiles of the normalised temperature increase (left) and of the normalised velocity (right) at gap outlet for case 32.

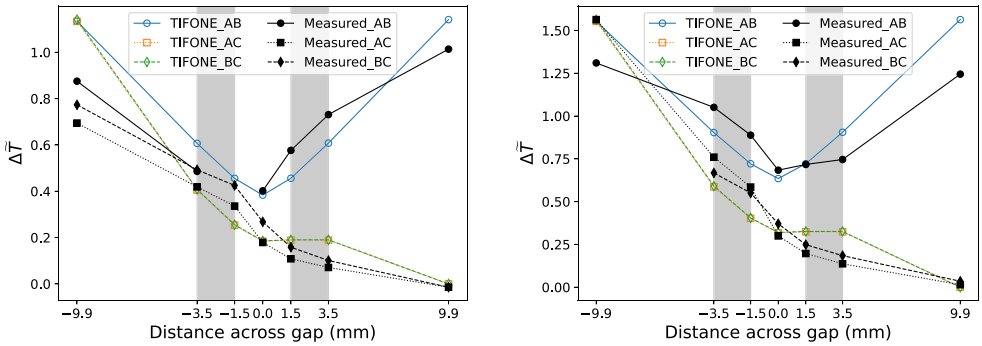

Fig. 25. Computed and measured radial distributions of the normalised temperature increase around the gap region at axial locations 393 mm (left) and 524 mm (right), for case 32. The shaded grey area indicates the radial extension of the wrapper.

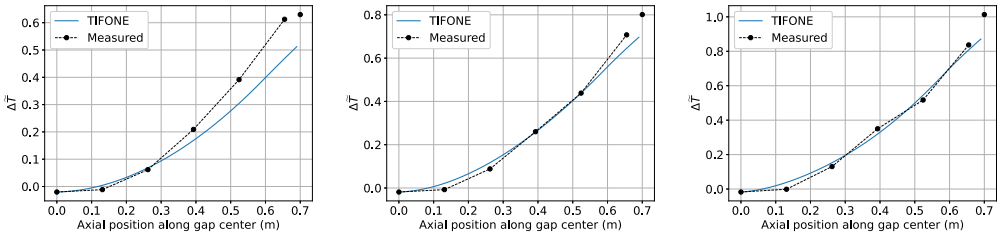

Fig. 26. Computed and measured axial evolution of the normalised temperature increase at the centre of the IW region for cases 34 (left), 36 (centre) and 38 (right).

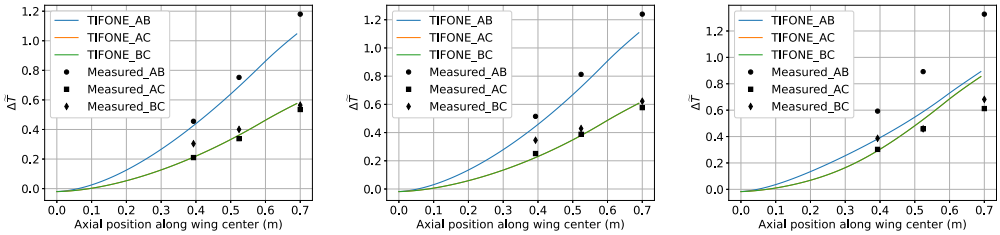

Fig. 27. Computed and measured axial evolution of the normalised temperature increase at the centre of each gap for cases 34 (left), 36 (centre) and 38 (right).

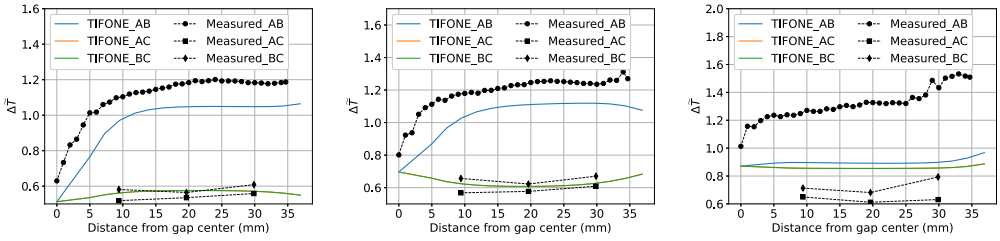

Fig. 28. Computed and measured profiles of the normalised temperature increase at gap outlet for cases 34 (left), 36 (centre) and 38 (right).

normalised temperature increase at radial locations for which measurements are available. The quantitative features are followed by the simulations even better than in previous cases, especially for what concerns assembly C, which is likely associated to the fact that the presence of the wire has a negligible effect for an unheated assembly.

For the three further cases here considered, characterised by a progressive reduction in the IW coolant flow rate, the axial evolution of the normalised temperature increase is again reasonably well reproduced, see Figs. 26 and 27. Fig. 28 also shows a good agreement on the profile of the normalised temperature increase along the AB gap for cases 34 ($\widetilde{Y}_{mix}$ = 1.3) and 36 ($\widetilde{Y}_{mix}$ = 2.1). Case 38, instead, is characterised by $\widetilde{Y}_{mix}$ = 12 and indeed, as expected, TIFONE cannot reproduce the physical behaviour in this case.

4.7. Summary

It is convenient to summarise the results of the preliminary validation of TIFONE here presented, in terms of deviation of the computed values from the available measured ones. This can be regarded as a preparatory step towards the qualification of the code, following the approach already being adopted, e.g., for ANTEO+ (Lodi and Grasso, 2022).

The available validation domain involved only one specific geometrical configuration, characterised by a single corner. This means that future work is needed to qualify TIFONE in more reactor-relevant geometries. As far as Reynolds numbers are concerned, values between approximately 1400 and 6000 were considered. As for buoyancy

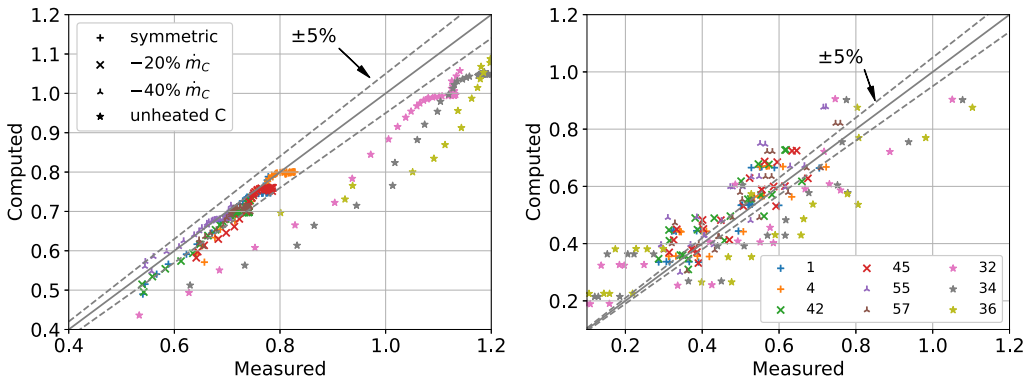

Fig. 29. Summary of validation results for cases with $\widetilde{Y}_{mix} \lesssim 2.5$: SC temperatures along gap AB (left) and wall temperatures (right). Different symbols are used for each set of cases (see legend on left plot), while different colours are used for each individual case (see legend on right plot).

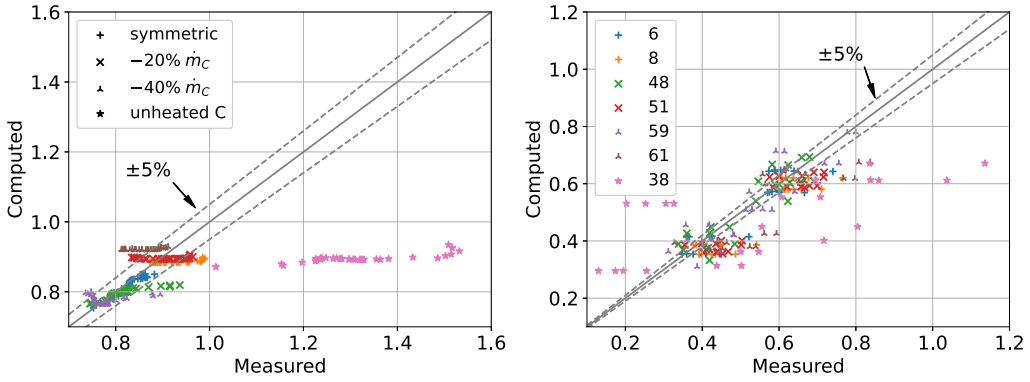

Fig. 30. Summary of validation results for cases with $\widetilde{Y}_{mix} > 2.5$: SC temperatures along gap AB (left) and wall temperatures (right). Different symbols are used for each set of cases (see legend on left plot), while different colours are used for each individual case (see legend on right plot).

effects, values of $\widetilde{Y}_{mix}$ between 0.9 and 20 were found, although it was observed that TIFONE only reproduces the experimental results reasonably well for $\widetilde{Y}_{mix} \lesssim 2.5$.

Fig. 29 shows a graphical summary of the comparison between computed and measured values for cases with $\widetilde{Y}_{mix} \lesssim 2.5$. Consistently with the rest of the paper, normalised temperature values $\Delta\widetilde{T}$ are considered. The left plot shows that the coolant temperature in the IW region is generally well described by TIFONE, with the exception of strongly asymmetric cases with unheated bundle C, where the simulation results are affected by the lack of a self-consistent coupling with ANTEO+. The right plot shows instead that results concerning wall temperatures are subject to a larger dispersion, which can be at least partially traced back to local effects associated to the presence of the wire, a feature which cannot be reproduced in ANTEO+ - and, consequently, in TIFONE.

Fig. 30 provides the same graphical summary for cases with $\widetilde{Y}_{mix} > 2.5$, for the sake of completeness. As expected, in these cases buoyancy effects dominate, causing a globally worse agreement.

Tables 6 and 7 summarise the results of the validation exercise in terms of maximum relative errors and standard deviations for cases with $\widetilde{Y}_{mix} \lesssim 2.5$ and $\widetilde{Y}_{mix} > 2.5$, respectively. It can be seen the overall reasonably good agreement with experimental data, and how SC temperatures increases are globally underestimated by the code, while the opposite is true for wall temperatures.

Table 6
Relative errors and standard deviations for TIFONE preliminary validation cases with $\widetilde{Y}_{mix} \lesssim 2.5$.

Quantity	Average relative error [%]	Standard deviation [%]
SC temperature	−6.026	8.485
Wall temperature	11.37	10.29

Table 7
Relative errors and standard deviations for TIFONE preliminary validation cases with $\widetilde{Y}_{mix} > 2.5$.

Quantity	Average relative error [%]	Standard deviation [%]
SC temperature	−4.604	16.86
Wall temperature	−3.015	10.92

5. Conclusions and perspective

In this paper, the design, development and preliminary validation of a new DOC, TIFONE, for the calculation of the IW flow and heat transfer in HLMCRs, were presented.

TIFONE provides a very fast solution of the full core IW flow and heat transfer in forced and mixed convection regime thanks to the adoption of the SC method and thanks to simplifying assumptions such as the neglection of pressure-driven cross-flows.

A preliminary validation campaign against IW experiments carried out on the THESYS loop at the KALLA facility confirmed the code capability to reproduce the measured coolant temperatures for forced and mixed convection regimes, up to $\widetilde{Y}_{mix} \lesssim 2.5$. This activity also pointed out several necessary improvements to the constitutive relations adopted in TIFONE. Specifically, the friction factor correlations adopted for corner SCs and the assumptions concerning inter-SC turbulent momentum exchange should be revised, possibly via dedicated experiments and/or DNS calculations.

On a longer time scale, the development of a full core TH code capable of self-consistently solving the TH for each SA accounting for the IW flow and heat transfer will be pursued. The simplest way to tackle this is to couple TIFONE with multiple instances of ANTEO+.

Another possibility is to couple TIFONE to the TH module of FRENETIC, a multi-physics (NE+TH) code for steady-state and transient analyses of LMCRs, which features a 1D TH solution within each SA (Nallo et al., 2020) - although in this case the radial detail within each SA would be lost.

Finally, as far as the code qualification is concerned, two lines of activity are foreseen:

(a) A benchmark against CFD simulations performed adopting the porous medium approach and considering the ATHENA facility is foreseen, to test TIFONE in a more reactor-relevant geometry (LR-D-S-190, 2015; Cioli Puviani et al., 2024). Another possibility is to compare the TIFONE results presented in this paper against CFD simulations performed for the same experimental setup here considered (Uitslag-Doolaard et al., 2019), to shed light on the origin of the discrepancies with respect to experimental data.

(b) Other facilities including IW flow and heat transfer effects are planned, including CLEAR-S and ATHENA itself. The resulting datasets shall be employed for further validating TIFONE, with specific focus on effects associated with multi-SA configurations (Wu, 2016). Instead, experiments performed in the PLANDTL facility (see Nishimura et al., 2000) cannot be employed to further validate TIFONE, since the physical situation realised in these experiments falls outside the TIFONE application domain. Indeed, the latter is limited to cases where the IW gap is fed from the bottom as a result of a bypass of the core mass flow rate, resulting in a dominant axial velocity component, while in PLANDTL experiments the IW flow resulted from buoyancy-driven lead motion between the inter-wrapper region itself and the upper plenum.

CRediT authorship contribution statement

G.F. Nallo: Writing – review & editing, Writing – original draft, Visualization, Software, Methodology, Investigation, Formal analysis, Data curation. **F. Lodi:** Writing – review & editing, Supervision, Software, Methodology, Investigation, Formal analysis, Data curation, Conceptualization. **G. Grasso:** Writing – review & editing, Supervision, Project administration, Methodology, Investigation, Funding acquisition, Conceptualization.

Declaration of competing interest

The authors declare that they have no known competing financial interests or personal relationships that could have appeared to influence the work reported in this paper.

Data availability

Data will be made available on request.

Acknowledgements

The authors would like to express their gratitude to Dr. M. Tarantino (ENEA, SESAME coordinator) and Dr. J. Pacio (SCK CEN, leader of the KALLA experiment) for having provided the data obtained in the IW flow and heat transfer experiments performed during the SESAME project, which were used for the validation here presented. This work was performed within the framework of a research contract by ENEA, which contributed to funding the PhD of one of the authors, G.F.N.

References

Basehore, K.L., Todreas, N.E., 1980. Superenergy-2: A Multiassembly, Steady- State Computer Code for LMFBR Core Thermal-Hydraulic Analysis. Technical Report, DOE, Richland, WA.

Blasius, P.R.H., 1913. Das aehnlichkeitsgesetz bei reibungsvorgangen in flussigk eiten. Forschungsheft 64, 1–41. http://dx.doi.org/10.1007/978-3-662-02239-9, URL: http://link.springer.com/10.1007/978-3-662-02239-9.

Chen, S.-k., 1984. Constitutive Correlations for Wire-Wrapped Subchannel Analysis Under Forced and Mixed Convection Conditions (Ph.D. thesis). Massachussets Institute of Technology, p. 543.

Cioli Puviani, P., Di Piazza, I., Marinari, R., Zanino, R., Tarantino, M., 2024. Multiscale thermal-hydraulic analysis of the ATHENA core simulator. Nucl. Technol. 210 (4), 692–712. http://dx.doi.org/10.1080/00295450.2023.2215682.

Colebrook, C.F., 1939. Turbulent flow in pipes, with particular reference to the transition region between the smooth and rough pipe laws. J. Inst. Civ. Eng. 11 (4), 133–156. http://dx.doi.org/10.1680/ijoti.1939.14509.

Deng, J., Lu, Q., Wu, D., Wang, C., Guo, C., Mi, Z., Huang, D., Yan, M., Wang, X., Chen, X., Li, P., 2020. Sub-channel code development of lead-bismuth eutectic fast reactor available for multiple fuel assembly structures. Ann. Nucl. Energy 149, 107769. http://dx.doi.org/10.1016/j.anucene.2020.107769, URL: https://www.sciencedirect.com/science/article/pii/S0306454920304679.

Duchatelle, L., Vautrey, L., 1964. Determination des coefficients de convection d'un alliage NaK en ecoulement turbulent entre plaques planes paralleles. Int. J. Heat Mass Transfer 7, 1017–1031. http://dx.doi.org/10.1021/cen-v035n051.p050a.

Dwyer, O.E., 1965. Heat transfer to liquid metals flowing turbulently between parallel plates. Nucl. Sci. Eng. 21 (1), 79–89. http://dx.doi.org/10.13182/nse65-a21017.

George, T.L., Basehore, K.L., Prather, W.A., 1980. Cobra-WC Model and Predictions for Afast-Reactor Natural-Circulation Transient. Technical Report, Richland, WA.

Haaland, S.E., 1983. Simple and explicit formulas for the I friction factor in turbulent pipe flow. J. Fluids Eng. 105, 89–90. http://dx.doi.org/10.1115/1.3240975.

IAEA, 2012. Structural Materials for Liquid Metal-Cooled Fast Reactor Fuel Assemblies - Operational Behaviour, Nuclear Energy Series No. NF-T-4.3. Technical Report, Vienna.

Idelchik, I.E., 2007. Handbook of Hydraulic Resistance, fourth Editio Begell House, Redding, p. 914.

ISO 12207:2017, 2017. Systems and Software Engineering – Software Life Cycle. Standard, 2017, International Organization for Standardization, Geneva, CH.

Jackson, J.D., 1983. Turbulent mixed convection heat transfer to liquid sodium. Int. J. Heat Fluid Flow 4 (2), 107–111. http://dx.doi.org/10.1016/0142-727X(83)90011-5.

Kawamura, H., Ohsaka, K., Abe, H., Yamamoto, K., 1998. DNS of turbulent heat transfer in channel flow with low to medium-high Prandtl number fluid. Int. J. Heat Fluid Flow 19, 482–491.

Kays, W.M., Leung, E.Y., 1963. Heat transfer in annular passages - hydrodynamically developed laminar flow with arbitrarily prescribed wall temperatures or heat fluxes. Int. J. Heat Mass Transfer 6, 537–557. http://dx.doi.org/10.1016/0017-9310(63)90124-8.

Liang, Y., Chen, Y., Zhang, D., Liu, X., Deng, J., Wang, C., Tian, W., Qiu, S., Su, G.H., 2021. Experimental and numerical investigation on flow characteristics of inter-wrapper channel in LMFBR. Ann. Nucl. Energy 151, http://dx.doi.org/10.1016/j.anucene.2020.107918.

Lodi, F., 2017. Development of Core Design Methods and Tools for Gen-IV Heavy Liquid Metal Cooled Reactors (Ph.D. thesis). Alma Mater Studiorum Universit'a di Bologna, pp. xlii – 324.

Lodi, F., Grasso, G., 2016. ANTEO+: A subchannel code for thermal-hydraulic analysis of liquid-metal cooled systems. Nucl. Eng. Des. 301, 128–152.

Lodi, F., Grasso, G., 2017. Extension of the sub-channel code ANTEO+ to the mixed convection regime. Nucl. Eng. Des. 322 (September), 368–378. http://dx.doi.org/10.1016/j.nucengdes.2017.07.018.

Lodi, F., Grasso, G., 2022. Road to qualification of the ANTEO+ sub-channel code. In: Proc. Technical Meeting on State-of-the-Art Thermal Hydraulics of Fast Reactors, ENEA Brasimone Research Centre, Camugnano, Italy, 26–30 September 2022. International Atomic Energy Agency.

LR-D-S-190, 2015. Technological Installation of ATHENA and CHEM-LAB, Internal Report. Technical Report, ENEA.

Luo, X., Duan, W., Pan, R., Zhang, K., Ding, T., Chen, H., 2022. Whole core thermal-hydraulic analysis considering inter-wrapper flow phenomena in the liquid metal cooled fast reactor. Prog. Nucl. Energy 154, 104476. http://dx.doi.org/10.1016/j.pnucene.2022.104476, URL: https://www.sciencedirect.com/science/article/pii/S014919702200350X.

Mochizuki, H., 2007. Inter-subassembly heat transfer of sodium-cooled fast reactors: validation of the NETFLOW code. Nucl. Eng. Des. 42, 2040–2053.

Nallo, G., Abrate, N., Dulla, S., Ravetto, P., Valerio, D., 2020. Neutronic benchmark of the FRENETIC code for the multiphysics analysis of lead fast reactors. Eur. Phys. J. Plus 135, 238. http://dx.doi.org/10.1140/epjp/s13360-020-00171-8.

NEA, 2015. Handbook on Lead-bismuth Eutectic Alloy and Lead Properties , Materials Compatibility , Thermal- hydraulics and Technologies, 2015 ed. NEA, p. 950.

Nishimura, M., Kamide, H., Hayashi, K., Momoi, K., 2000. Transient experiments on fast reactor core thermal-hydraulics and its numerical analysis: Inter-subassembly heat transfer and inter-wrapper flow under natural circulation conditions. Nucl. Eng. Des. 200 (1), 157–175. http://dx.doi.org/10.1016/S0029-5493(99)00324-6, URL: https://www.sciencedirect.com/science/article/pii/S0029549399003246.

Pacio, J., Abdallah, B., Daubner, M., Fellmoser, F., Wetzel, T., 2018. D2.12 - KALLA Inter-Wrapper Flow Experiments. Technical Report, KIT, p. 120.

Pacio, J., Daubner, M., Fellmoser, F., Wetzel, T., 2019. Experimental study of the influence of inter-wrapper flow on liquid-metal cooled fuel assemblies. Nucl. Eng. Des. 352, 110145. http://dx.doi.org/10.1016/j.nucengdes.2019.06.007, URL: https://www.sciencedirect.com/science/article/pii/S0029549319301517.

Sadatomi, M., Sato, Y., Saruwatari, S., 1982. Two-phase flow in vertical noncircular channels. Int. J. Multiph. Flow 8 (6), 641–655. http://dx.doi.org/10.1016/0301-9322(82)90068-4.

Sleicher, C.A., Rouse, M.W., 1975. A convenient correlation for heat transfer to constant and variable property fluids in turbulent pipe flow. Int. J. Heat Mass Transfer 18 (5), 677–683. http://dx.doi.org/10.1016/0017-9310(75)90279-3.

Todreas, N.E., Kazimi, M.S., 1990. Nuclear Systems II - Elements of Thermal Hydraulic Design. Corporation, Hemisphere Publishing, p. 506.

Uitslag-Doolaard, H., Roelofs, F., Pacio, J., Batta, A., 2019. Experiment design to assess the inter-wrapper heat transfer in LMFR. Nucl. Eng. Des. 341, 297–305. http://dx.doi.org/10.1016/j.nucengdes.2018.11.019, URL: https://www.sciencedirect.com/science/article/pii/S0029549318307118.

Wu, Y., 2016. CLEAR-S: An integrated non-nuclear test facility for China lead-based research reactor. Int. J. Energy Res. 40 (14), 1951–1956. http://dx.doi.org/10.1002/er.3569, arXiv:https://onlinelibrary.wiley.com/doi/pdf/10.1002/er.3569, URL: https://onlinelibrary.wiley.com/doi/abs/10.1002/er.3569.

Yang, W.S., Yacout, A.M., 1995. Assessment of the SE2-ANL code using EBR-II temperature measurements. URL: https://www.osti.gov/biblio/78595.

Yue, N., Zhang, D., Chen, J., Song, P., Wang, X., Wang, S., Qiu, S., Su, G., Zhang, Y., 2018. The development and validation of the inter-wrapper flow model in sodium-cooled fast reactors. Prog. Nucl. Energy 108, 54–65. http://dx.doi.org/10.1016/j.pnucene.2018.05.007, URL: https://www.sciencedirect.com/science/article/pii/S014919701830132X.